

NONDESTRUCTIVE PHOTOELASTIC CHARACTERIZATION OF
MONOCRYSTALLINE SILICON PHOTOVOLTAIC WAFERS

BY

LOGAN PERRIS ROWE

THESIS

Submitted in partial fulfillment of the requirements
for the degree of Master of Science in Mechanical Engineering
in the Graduate College of the
University of Illinois at Urbana-Champaign, 2018

Urbana, Illinois

Advisers:

Professor Harley T. Johnson
Dr. Gavin P. Horn

Abstract

Silicon wafers produced for the photovoltaic industry are becoming thinner. This renders the wafers more susceptible to bow under thermal residual and wafer handling stresses. Furthermore, a saw damage layer exists on the top and bottom surface of each wafer as a result of slicing the silicon ingot into wafers via a wire saw. Thinner wafers are more prone fracture under the combination of residual stress and external loads acting on microcracks in the saw damage layer. This research presents a novel method for characterizing monocrystalline silicon wafers using a photoelastic imaging technique that is capable of measuring the bulk residual stress fields in silicon wafers as well as locally elevated stress fields near microcracks.

Infrared photoelastic (PE) imaging is used to reveal the bulk residual stress field of each wafer and locally elevated stress field around each defect. The defect stress fields are first classified by using a support vector machine learning algorithm. The measured local and bulk residual stress fields around each defect are analyzed in order to characterize each crack according to its stress intensity factors. The distribution of cracks on each wafer is subjected to a virtual uniaxial tensile load where the wafer strength is determined by the load at which the first crack is expected to propagate. The distribution of wafer strengths is used to calculate the expected Weibull parameters for the wafer set, under a pure tensile load.

Since the method is nondestructive, it can be used to calculate and compare the expected Weibull parameters for the same set of wafers under a variety of externally applied loads. The variation in wafer strength when loaded parallel and perpendicular to the direction of wire motion is in agreement with experimental observations. With the proper modifications to the experimental setup, using this method it is possible to rapidly and accurately characterize large batches of wafers in an automated way.

Table of contents

List of figures.....	v
List of tables.....	vii
List of abbreviations.....	viii
Nomenclature.....	ix
Chapter 1 – Introduction.....	1
1.1 Motivation.....	1
1.2 Thesis outline.....	2
Chapter 2 – Wafer slicing and inspection methods.....	4
2.1 Wafer slicing.....	4
2.2 Wafer etching.....	5
2.3 Inspection methods.....	5
2.3.1 Characterization by wafer bow.....	6
2.3.2 Microcrack detection via IR transmission.....	6
2.3.3 Microcrack detection via photoluminescence.....	7
2.3.4 Raman spectroscopy.....	7
2.3.5 Acoustic inspection.....	8
2.3.6 Load testing.....	8
2.3.7 Photoelastic imaging.....	9
Chapter 3 – Infrared photoelastic imaging.....	11
3.1 Infrared grey-field polariscope.....	11
3.2 Photoelastic experimental measurements.....	14
Chapter 4 – Machine learning and image processing.....	17
4.1 Data collection.....	17
4.2 Image processing.....	17
4.3 Classifying Defects via machine learning.....	20
Chapter 5 – Characterization of microcracks.....	23
5.1 Analysis of surface cracks.....	23
5.2 Theoretical local retardation field.....	25
5.3 Calculating the biaxial stress state near microcracks.....	28
5.4 Crack Geometric Factor.....	31
Chapter 6 – Characterization of wafer strength.....	32
6.1 Weibull statistics.....	32

6.2 Calculated wafer strength	34
6.3 Results and discussion	35
Chapter 7 – Conclusions and future work	41
7.1 Concluding statements	41
7.2 Future improvements	43
List of references.....	45
Appendix – Hypersensitive pixels	49

List of figures

Figure 3.1 Schematic of the infrared grey-field polariscope. [Adapted from [22]]	11
Figure 3.2 The direction of first principal strain bisects the major and minor axes on the polarization ellipse. [Adapted from [34]].....	13
Figure 3.3 Retardation caused by the stress field near a crack tip forms a bowtie pattern. The bowtie will consistently change orientation between the shear 0 (a) and shear 45 (b) images. For bowties caused by microcracks, the orientation in the shear max image (c) depends on the ratio of stress intensity factors of the microcrack. Microcracks are too thin to be observed in IRT images (d) but cracks sometimes emanate from indentations caused by LAWS, which appear as dark spots in the IRT image.....	15
Figure 4.1 (a,b) Raw shear 0 and shear 45 retardation images with a faint background bowtie caused by the optic path and lines in shear 45 image caused by the detector. (c,d) The same shear 0 and shear 45 images after removing aberrations with a subtraction image while preserving locally elevated retardation fields.	19
Figure 4.2 Each plot compares the normalized measured local shear max profile to the best matching local shear max profile of a theoretical crack tip with crack plane orientation α and bulk biaxial stress ratio η listed in the title, where the bulk first principal stress direction is a known, measured value.....	20
Figure 4.3 Microscopic shear 0 image of an as-cut monocrystalline silicon wafer. Bowties that have been identified by the support vector classifier are boxed. Circled dark features are dust particles that had settled on the wafer surface.....	22
Figure 5.1 Retardation caused by the theoretical stress field near a typical surface crack.	24
Figure 5.2 The local shear max profile of a measured bowtie (a) is compared to the best matching profile of a theoretical bowtie (b). Every profile consists of the average values of a 20 μm radius line scan swept in a full circle around a bowtie. The observed difference in bowtie size is because in (a), when more than 30 μm from the crack tip, the local retardation becomes small compared to the bulk retardation and system noise while in (b) there is no bulk retardation or noise.....	27
Figure 5.3 Difference in principal stress field for 4 etched (100) Cz-Si wafers that are 176 μm thick. Axial direction of wire saw is vertical in each image and odd numbered wafers are rotated 180 degrees from even numbered wafers. The wafers shown here are typical samples from the batch of wafers evaluated in this study. The horizontal striation pattern is a result of the raster scan imaging process.	29
Figure 6.1 Weibull plot of wafer strengths for a uniaxial tensile load applied along ψ . The difference in strength observed in (a) likely stems from the distribution of flaw orientations which shows that a larger portion of flaws are approximately orthogonal to $\psi = 135^\circ$. The difference in strength observed in (b) may result from the direction of first principal stress in the saw damage layer. The magnitude of compressive residual stress is less along $\psi = 90^\circ$ resulting in a lower applied stress required to initiate failure.	35
Figure 6.2 Dependence of the characteristic strength and Weibull shape parameter on the direction of applied loading for a range of assumed saw damage layer thicknesses.	36

Figure 6.3 (a) Histogram of crack plane orientations. Population shown consists of microcracks that match the theoretical local shear max profile with the least amount of error. (b) Histogram of direction of the bulk first principal stress from a typical wafer..... 37

Figure 6.4 Distribution of crack geometric factors for the microcracks used to characterize the strength of each wafer. The secondary x axis represents the microcrack length assuming the crack is semicircular in shape. The geometric factors were calculated under the assumption that the saw damage layer is 12 μ m thick..... 39

Figure 7.1 Diminishing distinguishability of bowties as resolution is decreased. 43

List of tables

Table 1 Weibull parameters for wafers loaded parallel and perpendicular to the direction of wire motion; lines with bold text indicate data from this study.	36
--	----

List of abbreviations

DWS	Diamond wire saw
GFP	Grey-field polariscope
ID	Inner diameter
IR	Infrared
IRT	Infrared Transmission
LAWS	Loose abrasive wire saw
LP	Linear polarizer
ML	Machine learning
PE	Photoelastic
PL	Photoluminescence
PV	Photovoltaic
QWP	Quarter wave plate
RUV	Resonance ultrasound vibration
SAM	Scanning acoustic microscopy
SVC	Support vector classifier

Nomenclature

α	Orientation of crack plane with respect to the [100] direction
$\beta_{(loc)}^{(1)}$	First principal stress direction at a point in the crack tip stress field
$\beta_{(\infty)}^{(1)}$	First principal stress direction of bulk stress field
C_{θ}	Stress-optic coefficient along in-plane angle θ
χ	Crack geometric factor
δ	Linear retardation
$\bar{\delta}$	Average linear retardation across an image
Δ	Phase retardation
η	Ratio of bulk principal residual stresses
\bar{I}	Light intensity normalized by the average light intensity measured by the IR-GFP
K_{IC}	Fracture toughness
K_I, K_{II}	Mode I and mode II stress intensity factors
λ	Wavelength of light
$\bar{\lambda}$	Weibull location parameter
n_i	Refractive index along axis i
n	Order in which a wafer failed
N	Total number of wafers in the set
ω	Analyzer position with respect to the [100] direction
P_S	Probability of survival of a wafer
P_F	Probability of failure of a wafer
ϕ	Angle between the wafer surface and location on the crack front
$\pi_{11}, \pi_{12}, \pi_{44}$	Piezo optic coefficients
ψ	Angle of applied virtual tensile load with respect to the [100] direction
r	Radius from the crack tip
ρ	In-plane radius from the crack tip
$\sigma^{(i)}$	i^{th} principal stress
$\Delta\sigma_{(\infty)}$	Difference in bulk principal stresses
$\sigma_C^{(appl)}$	Applied tensile stress at which wafer is expected to fail
t	Wafer thickness
t_{sd}	Saw damage layer thickness
θ	In-plane angle from the crack tip

Chapter 1 – Introduction

1.1 Motivation

Crystalline silicon is the leading substrate used in solar cells today and accounts for over 85% of the global PV market [1, 2]. The increasingly competitive nature of the industry has driven solar cell manufacturers to seek new methods of reducing the overall cost of producing photovoltaic (PV) cells. Approximately one quarter of the total production cost goes toward materials and manufacturing the silicon wafer [3]. As such, costs can be reduced by decreasing the thickness of silicon substrates in order to obtain more wafers per ingot [4, 5, 6, 7].

Given the brittle nature of silicon, thinner wafers are more prone to fracture, which is a common occurrence during wafer handling steps and throughout the solar cell production process. This is particularly costly if a wafer fractures during the screen printing stages, which are later in the production process, requiring the operator to stop the production line to clean off aluminum paste and wafer shards [8]. The presence of residual stress and defects within the wafers increases the likelihood of fracture and can reduce the production yield by up to 25 percent [8]. Between 5 and 15 percent of wafers fail during production due to defects such as microcracks [1, 9, 10, 11].

Residual stress in the wafers arises because of radial temperature gradients that are present during the ingot cooling process. When the ingot is sliced into wafers the residual stress can relax by causing out-of-plane deformation in the wafer; this is known as wafer bow. Thinner wafers are more susceptible to out-of-plane deformation and thus experience more bow. Wafers with large bow are more likely to fail during wafer handling. Inline inspection techniques are often used to monitor wafer bow and identify wafers that are likely to fail during the production process. However, the root cause of wafer failure is not wafer bow, but rather a surface microcrack that when loaded in tension will propagate unstably [10, 12].

This thesis describes a method for characterizing the strength of monocrystalline silicon wafers based on the distribution of surface microcracks that have been identified in shear stress images taken by an infrared grey-field polariscope (IR-GFP). Czochralski grown, etched, Si (100) wafers are imaged at 5.5 μm resolution. A supervised machine learning algorithm identifies elevated shear stress patterns that are caused by microcracks. The shear stress field near each microcrack is decoupled into bulk shear stress in the wafer and locally elevated shear stress caused by the crack tip; both are analyzed in order to characterize each microcrack. The distribution of microcracks in each wafer is subjected to a virtual uniaxial tensile load and each wafer is characterized according to the stress at which the first crack is expected to propagate.

The analysis method presented here demonstrates the characterization of silicon wafers according to the flaws directly responsible for wafer failure. Using the experimental setup in its current state, the time required to image each wafer precludes this analysis method from being adapted as an inline inspection technique. However, unlike other crack detection methods, this method characterizes microcracks by their stress field, which is an order of magnitude larger than the microcracks themselves, and thus significantly reduces the resolution requirements. As such, with the proper modifications to the experimental setup, the analysis method described here may serve to improve upon existing inline inspection techniques.

1.2 Thesis outline

The following chapters cover existing photovoltaic (PV) wafer manufacturing and characterization techniques, the basic theory behind photoelastic PV wafer inspection, the methods developed and used in this study, and the results and potential future applications of the presented methods.

Chapter 2 discusses current wafer slicing technologies, the resulting saw damage layer, and the saw damage removal process. Also provided is an overview of several inspection methods used for the early detection of microcracks and wafer strength characterization.

Chapter 3 presents the theory behind the use of photoelastic (PE) imaging to study residual stress in PE materials. It also presents the infrared PE microscopic imaging setup used in this experiment to observe both bulk residual and locally elevated stress fields in PV wafers.

Chapter 4 presents the data collection and post processing techniques used when measuring the stress field of each PV wafer at high resolution. It also presents a supervised machine learning (ML) approach to identify locally elevated stress fields caused by surface microcracks.

Chapter 5 computes the theoretical PE image of a surface microcrack in a stressed PV wafer based on ideal crack tip stress fields. A method for characterizing microcracks by comparing the theoretical PE image to the measured PE image is shown. It also presents a method for calculating the expected biaxial stress state that relates the measured bulk stress field and characterized microcrack to the measured locally elevated stress field.

Chapter 6 introduces weakest link theory and discusses how Weibull statistics is used to characterize each wafer according to its expected strength as determined by the distribution of microcrack stress intensity factors. The dependence of wafer strength on the direction of an applied virtual tensile load is shown and compared to experimental observations. The distribution of microcrack geometric factors and lengths is also shown. This chapter also discusses the limitations of the presented method and how the limitations affect the final results.

Chapter 7 summarizes the strengths and challenges of the presented method for characterizing PV wafers according to the distribution of microcracks. Recommendations for improvements to the method and potential future applications are discussed.

Chapter 2 – Wafer slicing and inspection methods

The process of producing solar cells with a low probability of mechanical failure is three-fold. The first step is to minimize the residual stress and saw damage when forming wafers. The second step is to remove the damage that is inevitably caused, and the third step is to identify and recycle wafers that have an unacceptable level of remaining damage. Materials and production of silicon wafers accounts for approximately one quarter of the total production cost of silicon solar cells [3]. In the Czochralski growth method, several hundred wafers are sliced from each cylindrical ingot. However, during the wafer slicing process, approximately 50 percent of the material is lost to kerf. In an effort to reduce the amount of kerf produced, thinner slices are used to form the wafers. Initially this process was done by an inner diameter (ID) saw, which was not only a slow process since wafers were cut one at a time, but it also led to excessive wafer warpage and non-uniform thickness caused by flexing of the thin blade [13]. Now the preferred method of slicing an ingot is to use a wire saw, whereby a large portion of an ingot can be sliced into several hundred wafers simultaneously.

2.1 Wafer slicing

The two leading methods of wire saw slicing are loose abrasive slurry wire saw slicing (LAWS) and diamond wire saw slicing (DWS). Both are in use today but the latter is gradually becoming the primary method. A key difference between the two methods is the cutting mechanism. LAWS relies on rolling silicon carbide grains in a slurry of oil or ethylene glycol to remove material while DWS relies on a fixed diamond grit to remove material. The two cutting mechanisms are described in greater detail in [14]. The wire saw slicing process introduces damage to the top and bottom layer of the silicon wafer in the form of residual stress and microcracks. The length of cracks generated by each cutting mechanism depends on the size of the particles used to remove material [15]. DWS has been observed to produce shorter microcracks and a thinner saw damage layer while LAWS produces a lower density of microcracks [13, 14, 16]. Furthermore, DWS leaves a characteristic wire striation pattern along the direction of wire motion while damage caused by LAWS leaves pits in the wafer surface. As a result of the striation pattern, DWS

wafers have shown a substantial reduction in strength when loaded perpendicular to the direction of wire motion [17]. As a result, DWS wafers are generally weaker (stronger) than LAWS wafers when loaded parallel (perpendicular) to the direction of wire motion. DWS also has the potential to cut through ingots at a faster rate than LAWS; both slice at a rate of approximately half a millimeter per minute [13].

2.2 Wafer etching

Regardless of precautions taken during the wafer slicing process, saw damage is present on every as-cut wafer. The damage is highly localized to the surfaces and edges of each wafer. In the case of LAWS (DWS) the saw damage layer is estimated to be 25-40 (16-25) μm thick [18]. A grinding process can be used to smooth the edges while other post processing steps such as polishing and etching are used to remove some of the surface damage. Etching can be performed with either a caustic etch or an acid etch. The former produces a uniform thickness wafer with a rougher surface while the latter produces a smoother surface but less even thickness [19]. Etching away the saw damage layer asymptotically improves the mechanical strength of the wafer [5]. The amount of material that needs to be etched away depends on the depth of the saw damage layer, although in practice, typically only the top 10 to 20 μm of each surface are etched away and thus the entire saw damage layer is not removed [9, 10].

2.3 Inspection methods

The ideal inline inspection technique is fast, nondestructive, accurate, and robust. The technique must not hinder the rate of production or introduce damage to satisfactory wafers. Some techniques, such as characterizing wafers according to wafer bow, are rapid and nondestructive but do not detect microcracks that will ultimately initiate wafer failure. Other techniques such as scanning acoustic microscopy (SAM) and Raman spectroscopy are capable of detecting critical defects but require too much time per wafer to be considered inline inspection methods. The latter group of inspection methods is slow because of the high resolution required to detect critical microcracks, which are typically about 10 μm in length [12]. The wafer characterization method presented in this thesis currently falls into this group as well. However, since the method presented here characterizes wafers according to microcrack

stress fields, which are an order of magnitude larger than the cracks themselves, the resolution requirements to detect critical microcracks are much lower. Thus, with the proper modifications to the experimental setup this method has the potential to be considered as an inline inspection method. In the following subsections several techniques for assessing wafer damage and residual stress are outlined and their strengths and weaknesses are discussed.

2.3.1 Characterization by wafer bow

For Czochralski grown wafers, radial temperature gradients, present as the silicon melt solidifies to form an ingot, give rise to thermal residual stresses. When the ingot is sliced into wafers, the residual stress will relax by producing out-of-plane deformation, referred to as wafer bow. Wafers with a large diameter to thickness ratio are more susceptible to out-of-plane deformation, thus thin wafers are rendered more likely to bow [20]. Since the out-of-plane deformation is also proportional to the thermal residual stress in each wafer, qualitative assessments about wafer strength can be made by measuring wafer bow. Characterizing wafers by measuring out-of-plane deformation is rapid and nondestructive, but does not account for the defects that are directly responsible for initiating wafer failure.

2.3.2 Microcrack detection via IR transmission

Infrared transmission (IRT) imaging involves shining an IR beam through a silicon wafer. Defects such as cracks or precipitates in the wafer will interact with the light by either absorbing or reflecting the incident light and thus altering the observed intensity of the IR beam. While this technique requires wafers to have surfaces that are smoother than that of a typical PV wafer, it has been utilized in the identification of edge cracks in ribbon wafers [10]. The technique is fast and nondestructive but its use as an inspection tool for PV wafers is limited by cost effective surface preparation techniques and the inherently small size of microcracks. Additionally, cracks on Czochralski grown wafers often have a width that is smaller than the diffraction limit of IR light which renders them invisible in IRT images [1], as can be observed in Fig. 3.3.

2.3.3 Microcrack detection via photoluminescence

When an incident photon with an energy greater than the band gap energy excites an electron, the electron will temporarily enter the conduction band. After the carrier lifetime, the electron will recombine with a hole in the valence band and a photon with the same energy as the band gap will be emitted. This process is known as photoluminescence (PL) and the intensity of emitted light is proportional to the carrier lifetime and inversely proportional to the density of defect structures. As such, PL measurements of wafers are used as an early indicator of solar cell efficiency and PL measurements of silicon bricks are used to obtain spatially resolved carrier lifetime data prior to wafering [21, 22]. Cracks also serve as regions of increased recombination and are thus observed in PL images as having reduced intensity. However, grain boundaries, dislocations, and cracks all similarly reduce the emitted PL signal, so it is difficult to determine which structure is responsible for the reduction of a PL signal [23, 24]. While it has been observed that PL measurements reveal more detail about the geometry of a microcrack than can be observed in IRT images alone [23], the ability to identify microcracks in PL images is also limited by the size of the defects.

2.3.4 Raman spectroscopy

When a molecule is excited by an incident photon of energy $h\nu_i$ such that an electron is excited to a virtual energy state, the electron will rapidly return to a lower energy state and emit a photon of energy $h\nu_s$. The value of $h\nu_s$ is the difference in energy between the virtual and final energy state. Almost always, the incident and emitted photons will have the same energy; this process is called Rayleigh scattering [25, 26]. However, for approximately one in ten million photons, $h\nu_s$ is not equal to $h\nu_i$ [26]. To satisfy the conservation of energy, the difference in energies is accounted for by a change in the molecule's vibrational energy level [25]. When $h\nu_s$ is greater (less) than $h\nu_i$ the process is called anti-Stokes (Stokes) Raman scattering. Materials can be characterized according to the energies at which Stokes and anti-Stokes peaks occur; the sharpness of the Raman peaks is proportional to the material's crystallinity. In silicon, applying compressive (tensile) stress will cause the location of the Raman peak to

shift towards higher (lower) energy. Popovich et al. utilized these properties and Raman spectroscopy to study the saw damage layer of silicon wafers sliced by LAWS [27]. Using a biaxial stress assumption, a 500 MPa compressive stress was measured in the saw damage layer, and a layer of amorphous silicon was observed only in the smooth grooves of indentations [27]. Raman spectroscopy is nondestructive and capable of high spatial resolution, but it is limited by the penetration depth of light and can only measure the top few microns of the wafer surface.

2.3.5 Acoustic inspection

Two glasses, identical except that one that contains a crack, when struck will emit frequencies that are different enough to be detected by the human ear [1]. Similarly, a silicon wafer that contains a crack will resonate at a lower natural frequency and have a lower peak amplitude than a crack free wafer [1, 28]. Taking advantage of this effect, the resonance ultrasound vibration (RUV) technique requires approximately 3 seconds to inspect a wafer and is estimated to have submillimeter crack length sensitivity [29]. RUV uses a piezoelectric transducer to vibrate a silicon wafer; the vibrations give rise to longitudinal standing waves at the wafer's resonance frequencies that can be detected by an ultrasonic probe [29]. The band width and frequency of a prespecified mode in the ultrasonic frequency spectrum are broadened and reduced, respectively, when a millimeter scale crack is present in the wafer. By monitoring this mode defective wafers can be identified. Scanning acoustic microscopy may also be used to detect the presence of microcracks and is capable of detecting cracks as small as 5 to 10 μm in length [1, 30]. However, the time required to obtain a high resolution image of a wafer using SAM precludes the technique from being used for inline wafer inspection.

2.3.6 Load testing

One of the primary motivators behind evaluating the residual stress state and surface damage of a PV wafer is to determine whether it is likely to fracture during the cell fabrication process. Early detection is important because the further a defective wafer makes it through the production process, the greater the cost in the manufacturing process. One method of identifying low quality wafers is to load

test every wafer with tensile loads similar to those seen during the handling and the cell fabrication processes. Applying a uniform tensile load to a wafer is difficult since stresses induced by a gripping mechanism may themselves initiate fracture. As such, Sopori et al. have proposed a contact free method of preloading wafers [10]. This is accomplished by optically heating wafers to produce temperature gradients that result in tensile and compressive loads that simulate what each wafer might experience during the production process [10]. Wafers that fail under these loads would likely have failed during cell fabrication and can be recycled early in the process.

2.3.7 Photoelastic imaging

Photoelastic materials such as silicon and glass become birefringent when they experience a deviatoric stress; the birefringence is proportional to the in-plane difference in principal stresses. Birefringent materials have two distinct refractive indices that are oriented along the principal strain directions. The electric field vector of light that passes through the material is decomposed into orthogonal components oscillating along each principal strain direction. Upon transmission, the light is phase shifted thus changing its polarization state. A polariscope compares the incident and transmitted polarization states to produce an image of the induced phase shift, which directly relates to the in-plane shear stress.

The two standard types of polariscope are circular and planar. Circular polariscopes use circularly polarized light to reveal isochromatic fringes that are contours of constant difference in principal stress. Plane polariscopes use linearly polarized light to reveal isochromatic fringes, and isoclinic fringes that occur when either principal stress direction is aligned with the polarizer. A circular polariscope is often preferable since it is difficult to distinguish between isoclinic and isochromatic fringes without rotating or applying an external load to the specimen. Isochromatic fringes arise at phase retardations of $2\pi n$ where n is an integer. Residual stresses in thin silicon wafers produce phase retardations that are much smaller

than 2π and therefore do not give rise to fringes. In such cases where only sub-fringe retardations are present, a grey-field polariscope can be used to quantify the magnitude of shear stress.

The infrared grey-field polariscope is a mixed polariscope using a quarter wave plate ahead of the silicon wafer, like a circular polariscope, and a rotating analyzer between the wafer and detector, as depicted in Figure 3.1. The IR-GFP has proved to be an invaluable tool for a variety of silicon wafer characterization methods that rely on sub-fringe PE analysis. Lin et al. used the IR-GFP to obtain full field images of c-Si wafers, that provide information about both the thermal residual stress field and dislocation stress fields [31]. Inzinga et al. used the IR-GFP to characterize the stress concentrations at the corners of etched cavities in anodically bonded silicon wafers [32]. IR-GFP measurements are limited to measuring shear stress in a sample, however with additional information one can determine the full in-plane stress state. For instance, Ganapati et al. determined the complete in-plane stress state of macroscopic thermal residual stresses in a c-Si ribbon wafer by comparing shear stress measurements of the wafer before and after cleaving the wafer to create a free surface [33]. Furthermore, with the addition of a 5x microscope objective, the IR-GFP was used to detect β - SiC and β - Si₃N₄ particles embedded in mc-Si wafer; by comparing IR-GFP measurements with FEA simulations, the local and bulk birefringence patterns were decoupled and the residual stress field near the particle/matrix interface was assessed [33].

Enhanced resolution is crucial for not only for observing precipitate particles, but also for observing locally elevated stress fields. Locally elevated stress fields around microcracks are typically 60 to 80 μm in diameter and are not resolved in full wafer IR-GFP images. The IR-GFP setup used in this work and described in greater detail in chapter 3, also uses a 5x objective which increases its resolution to approximately 5.5 μm .

Chapter 3 – Infrared photoelastic imaging

Photoelastic analysis is used to measure the in-plane shear strain within a material. PE measurements are used to calculate the spatial distribution of difference in principal stresses as well as the direction of first principal stress. Conventionally PE is used to analyze thin plates of transparent birefringent materials. This chapter will describe the principles behind PE imaging and how we use the infrared grey field polariscope to obtain residual stress measurements in silicon wafers.

3.1 Infrared grey-field polariscope

The infrared grey-field polariscope consists of a halogen bulb light source, conditioned to be narrow band, which shines through a linear polarizer (LP) and a quarter wave plate (QWP). The result is circularly polarized light which passes through a rotating LP, known as the analyzer, and is collected by an infrared detector. As shown in Fig. 1, the object of interest, a silicon PV wafer, is placed between the analyzer and the QWP.

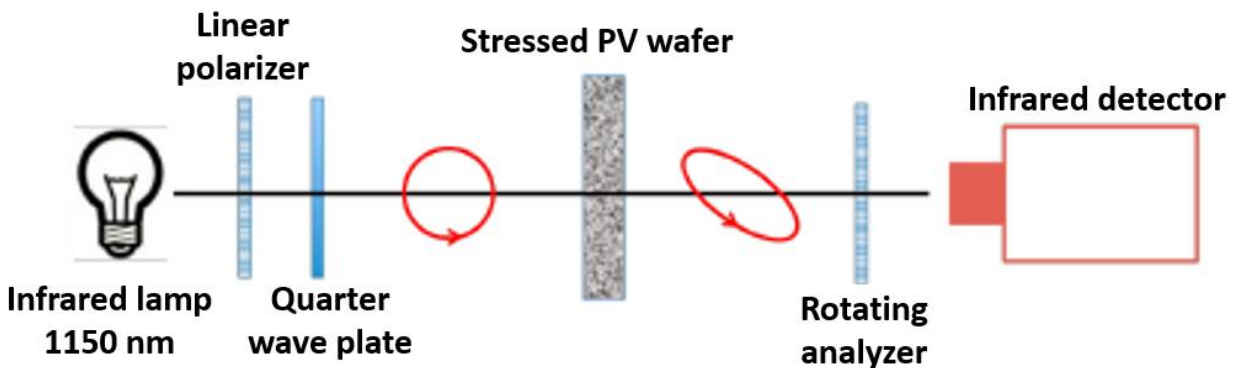


Figure 3.1 Schematic of the infrared grey-field polariscope. [Adapted from [22]]

The object must be birefringent, transparent, and is typically of uniform thickness. Birefringent materials exhibit an anisotropic optical property whereby the material will have a fast and slow axis. The electric field vector of light which passes through a birefringent material is decomposed into two orthogonal components, one that oscillates along the slow axis and the other along the fast axis. The component that oscillates along the slow axis of the material experiences a larger refractive index than the component of light that oscillates along the fast axis. Upon exiting the material the component of

light oscillating along the slow axis is retarded by the difference in optic path lengths (δ), which can be expressed as

$$\delta = t(n_e - n_o) \quad (3.1)$$

where n_o and n_e are respectively the ordinary and extraordinary refractive indices. When the retardation is between zero and one quarter of the wavelength of light used, the light will exit the material as elliptically polarized. Photoelastic materials such as glass and silicon only exhibit birefringence when they experience a difference in principal strains. The difference in principal strains alters the material's atomic spacing more along the first principal strain direction than along the second principal strain direction. This gives rise to anisotropic dielectric constants and therefore also anisotropic refractive indices. This relation can be expressed in terms of the difference in principal stresses,

$$n_1 - n_2 = C(\sigma^{(1)} - \sigma^{(2)}) \quad (3.2)$$

where C is the stress-optic coefficient, and $\sigma^{(1)}$ and $\sigma^{(2)}$ are in-plane principal stresses. In accordance with Eq. (3.1) and Eq. (3.2), in PE materials, the retardation depends on the magnitude of the difference in principal stresses and the thickness of the material. Thus the ellipticity of the light upon exiting the material also depends on the magnitude of difference in principal stresses. The IR-GFP determines the resultant polarization ellipse by measuring the light intensity at 16 distinct analyzer positions. When light passes through the analyzer, the electric field vector is split into orthogonal components that are aligned with and perpendicular to the analyzer position (ω); the former is transmitted while the latter is extinguished. Thus when the analyzer aligns with the major (minor) axis of the ellipse, the light intensity is at its brightest (dimpest). Upon measuring the light intensity at each analyzer position, a polarization ellipse is traced out.

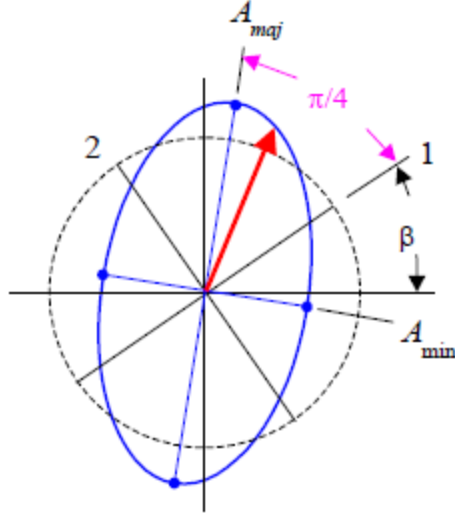


Figure 3.2 The direction of first principal strain bisects the major and minor axes on the polarization ellipse. [Adapted from [34]]

The first principal stress direction (β) is $\pi/4$ radians between the major and minor axes while the amplitude of oscillation is proportional to the difference in principal stresses. The fluctuation of measured light intensity as the analyzer rotates can be expressed as [22, 35]

$$\bar{I} = 1 + \sin(\Delta) \sin(2\omega - 2\beta) \quad (3.3)$$

where

$$\Delta = 2\pi \frac{\delta}{\lambda} \quad (3.4)$$

\bar{I} is the measured light intensity normalized by the average light intensity, and ω is the analyzer position.

Equation (3.3) can be expressed in terms of $\sin(2\omega)$ and $\cos(2\omega)$, [22, 35]

$$\bar{I} = 1 + \bar{I}_{cos} \cos(2\omega) + \bar{I}_{sin} \sin(2\omega) \quad (3.5)$$

where

$$\bar{I}_{cos} = -P \sin(\Delta) \sin(2\beta) \quad (3.6)$$

$$\bar{I}_{sin} = P \sin(\Delta) \cos(2\beta) \quad (3.7)$$

and P is the ratio of polarized light intensity to the average light intensity. Imperfections in the experimental setup such as the presence of unpolarized ambient light and depolarization of the light source due to scattering result in a P value that is less than one. Writing \bar{I} in terms of \bar{I}_{cos} and \bar{I}_{sin} is

convenient because \bar{I}_{\sin} (\bar{I}_{\cos}) is proportional to the difference in normal strains along the x-y ($\pm 45^\circ$) directions. Equations (3.1), (3.2), and (3.4) show that Δ is proportional to the product of the stress optic coefficient, sample thickness, and difference in principal stresses. When considering the case of residual stresses in thin silicon wafers, it is safe to assume that Δ is small and Eq. (3.6) and Eq. (3.7) can be reduced to

$$\bar{I}_{\cos} \cong -P\Delta \sin(2\beta) \quad (3.8)$$

$$\bar{I}_{\sin} \cong P\Delta \cos(2\beta) \quad (3.9)$$

3.2 Photoelastic experimental measurements

We use an infrared grey field polariscope to image each wafer and exploit the fact that silicon is both photoelastic and transparent to infrared light [35]. Using components from Eq. (3.1) and Eq. (3.2), linear retardation experienced by light passing through a stressed silicon wafer may be expressed in terms of the difference in principal stresses according to

$$\delta = C \int_0^t \sigma^{(1)} - \sigma^{(2)} dz \quad (3.10)$$

where t is the thickness of the wafer, $\sigma^{(1)}$ and $\sigma^{(2)}$ are the in-plane principal stresses, C is the stress optic coefficient, and z is the direction of light propagation. Variations in stress through the thickness of the wafer may be accounted for in the integral.

The light source for the IR-GFP used in this work is conditioned to be narrow band, circularly polarized, and centered at approximately 1150 nm. When circularly polarized light experiences a linear retardation as described in Eq. (3.10), the light gains an ellipticity proportional to the magnitude of shear stress in the wafer. The intensity of light is monitored by a charge coupled detector which resides behind a rotating analyzer. Thus the image is brightest when the analyzer aligns with the major axis of the polarization ellipse and the image is dimmest when it aligns with the minor axis of the ellipse.

The degree of ellipticity and orientation of the ellipse are determined via a lock-in algorithm which monitors the intensity of each pixel at 16 distinct analyzer angles. Since the degree of ellipticity is

proportional to the magnitude of shear strain, this can be used to calculate the shear strain due to x-y normal strains, the shear strain due to $\pm 45^\circ$ normal strains, and the maximum shear strain. A more in-depth summary of this instrument is given in the previous section. Because the measured ellipse is the result of the net retardation through the thickness of the wafer, when any variation in shear stress through the thickness of the wafer is present, the variation in the z direction must be accounted for in Eq. (3.10). This is the case for many microscopic flaws such as cracks or voids where the shear stress is greater near the flaw. As such, when observing microscopic flaws we refer to the net retardation caused by x-y shear stress (δ_0) and $\pm 45^\circ$ shear stress (δ_{45}) instead of the measured shear stress itself.

The spatial resolution of the IR-GFP can be increased to approximately $5.5 \mu\text{m}$ with the addition of a 5x objective. This allows us to resolve bowtie features in the δ_0 and δ_{45} images that result from locally elevated stresses. Examples are shown in Fig. 3.3 for a defect in a typical PV-grade crystalline silicon wafer with (001) orientation.

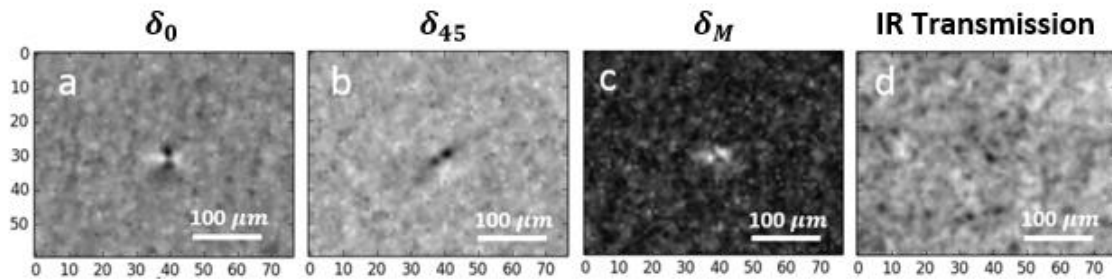


Figure 3.3 Retardation caused by the stress field near a crack tip forms a bowtie pattern. The bowtie will consistently change orientation between the shear 0 (a) and shear 45 (b) images. For bowties caused by microcracks, the orientation in the shear max image (c) depends on the ratio of stress intensity factors of the microcrack. Microcracks are too thin to be observed in IRT images (d) but cracks sometimes emanate from indentations caused by LAWS, which appear as dark spots in the IRT image.

Figures 3.3a and 3.3b are measured directly by the IR-GFP and the retardation observed in Figure 3.3c is proportional to the difference in principal stresses where δ_M is calculated according to

$$\delta_{45} = C_0 \int_0^t \sigma_{11} - \sigma_{22} dz \quad (3.11)$$

$$\delta_0 = -2C_{45} \int_0^t \sigma_{12} dz \quad (3.12)$$

$$\delta_M = C_\beta \int_0^t \sigma_{(1)} - \sigma_{(2)} dz = C_\beta \sqrt{\left(\frac{\delta_{45}}{C_0}\right)^2 + \left(\frac{\delta_0}{C_{45}}\right)^2} \quad (3.13)$$

$$\beta^{(1)} = \tan^{-1} \left(\frac{C_{45}\delta_{45}}{C_0\delta_0} - \frac{C_{45}}{\delta_0} \sqrt{\left(\frac{\delta_0}{C_{45}}\right)^2 + \left(\frac{\delta_{45}}{C_0}\right)^2} \right) \quad (3.14)$$

where $\beta^{(1)}$ is the direction of the first principal stress and C_θ is the stress optic coefficient for silicon in the (001) plane along angle θ from the [100] direction. Silicon has an anisotropic stress optic coefficient in the {100} family of planes. To calculate the stress optic coefficient, we used the piezo-optic coefficients determined in [36], given by

$$C_{(001)}(\theta) = \frac{n_0^3}{2} \left(\frac{\sin^2(2\theta)}{\pi_{44}^2} + \frac{\cos^2(2\theta)}{(\pi_{11} - \pi_{12})^2} \right)^{-\frac{1}{2}} \quad (3.15)$$

where $n_0 = 3.54$ is the ordinary refractive index, $\pi_{44} = 6.50 \cdot 10^{-13} \text{Pa}^{-1}$, and $\pi_{11} - \pi_{12} = 9.88 \cdot 10^{-13} \text{Pa}^{-1}$. We refer to $C_{(001)}\left(\frac{\pi}{4}\right)$ as C_{45} , $C_{(001)}(0)$ as C_0 , and $C_{(001)}(\beta^{(1)})$ as C_β .

Chapter 4 – Machine learning and image processing

Several thousand IR-GFP measurements (5x images) are taken of each wafer. Within these images exist bowtie patterns as shown in Figure 3.3. Many of the bowtie patterns result from residual stresses acting on a microcrack. This chapter describes the methods used to obtain and post-process the images for each wafer as well as the supervised machine learning (ML) approach used to identify bowtie features. Methods used to train and optimize the support vector classifier (SVC) will also be discussed.

4.1 Data collection

The IR-GFP used in this work is capable of recording one 640 by 480 pixel array for each δ field measurement. A full field image of a wafer has a spatial resolution of approximately 325 μm . As can be seen in Fig. 3.3, a resolution of at least 80 μm is required to resolve spikes in the δ field associated with the presence of a surface crack. The addition of the 5x objective provides 5.5 μm spatial resolution which permits not only resolution of locally elevated δ values but also the fluctuations in intensity around each bowtie pattern. The increased spatial resolution comes at the cost of a smaller field of view, approximately 3.5 by 2.6 millimeters. Thus over 3,000 images are required to obtain the full δ field of a 156 by 156 mm wafer at 5.5 μm resolution. The task of measuring each wafer's δ field has been automated by using an x-y stage, retrofitted with stepper motors, to raster scan each wafer across the optic path.

4.2 Image processing

As with any imaging system, imperfections in the light source, optic path, and detector can result in optical aberrations which are present in every image. Thus, a subtraction image is applied to the raw data to remove such optical aberrations. The subtraction image is generated according to

$$\delta^{(sub)} = \frac{1}{N_S} \sum_{i=1}^{N_S} \left(\delta_{(i)}^{(raw)} - \bar{\delta}_{(i)}^{(raw)} \right) \quad (4.1)$$

where $\delta_{(i)}^{(raw)}$ is the raw measured δ field, $\bar{\delta}_{(i)}^{(raw)}$ is the average value of the raw measured field, and in the case of this work, N_S is taken to be 108. The value of 108 is used because it is large enough to

sufficiently reduce the effect of locally elevated retardations on the subtraction image and small enough to exclude the wafer's bulk residual stress from the subtraction image. The location (density) of locally elevated stress fields in each etched wafer image is random (sparse), thus it is statistically unlikely that the same pixel (p) overlaps with more than one locally elevated stress field in N images. Thus p in the subtraction image is calculated from at most one locally elevated stress value (l) and at least $N_S - 1$ bulk stress values (b) and is approximately

$$p \cong \frac{l + b(N_S - 1)}{N_S} = \frac{l - b}{N_S} + b \quad (4.2)$$

When N_S is small, locally elevated stress fields have a large effect on the subtraction image. The images used to generate the subtraction image are those with the lowest average shear max values. Thus, when N_S is large, the subtraction image also contains the bulk residual stress field from the wafer; since the objective of the subtraction image is to only remove δ caused by optical aberrations, it is undesirable for bulk residual stress to be included in the subtraction image. The effects of applying a subtraction image can be observed in Fig. 4.1.

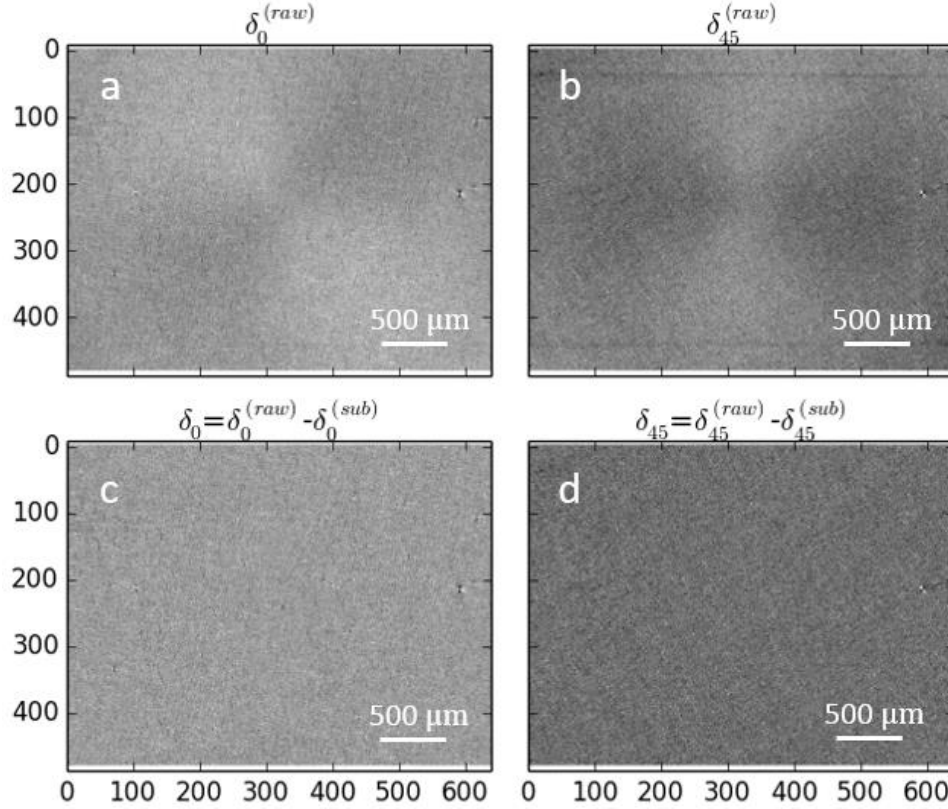


Figure 4.1 (a,b) Raw shear 0 and shear 45 retardation images with a faint background bowtie caused by the optic path and lines in shear 45 image caused by the detector. (c,d) The same shear 0 and shear 45 images after removing aberrations with a subtraction image while preserving locally elevated retardation fields.

Figure 4.1 gives confidence in our ability to remove optical aberrations from δ_0 and δ_{45} images without affecting the local δ fields. In accordance with Eq. (4.2), each δ field consists of locally elevated retardations, such as the bowtie features seen in Fig. 4.2, and bulk retardations. These are described by

$$\delta^{(loc)} = \delta - \bar{\delta} \quad (4.3)$$

$$\delta^{(\infty)} = \bar{\delta} \quad (4.4)$$

where $\bar{\delta}$ is the average value of the δ field and represents the retardation due to the wafer's bulk residual stress, which varies considerably across a full wafer but is nearly constant across each 5x image region. Hypersensitive pixels, defined as pixels that consistently register abnormally high values, are additional artifacts that also must be addressed during post-processing. The identification and removal of hypersensitive pixels is discussed in Appendix A.

4.3 Classifying Defects via machine learning

There are hundreds of resolvable bowtie defect features on each etched wafer and thousands on each as-cut wafer. There are many more that can be resolved at higher magnification, but it is only important to consider cracks that may initiate wafer fracture, so it is sufficient to observe only the population of cracks exhibiting the largest $\delta^{(loc)}$ field.

To identify most of these bowties, a support vector classifier is used to classify the profile of δ_0 and δ_{45} fields near locally elevated retardation levels as bowtie or non-bowtie. The profile of each δ field is measured by sweeping a 20 μm linescan in a circle around the point of maximum retardation. The average value of each linescan is recorded and then scaled to range from 0 to 1 as shown for $\delta_M^{(loc)}$ in Fig. 4.2. The theoretical $\delta_M^{(loc)}$ linescan is explained in more detail in chapter 5. The use of a swept 20 μm line scan is robust against variation in bowtie size since both small and large bowties produce similar profiles.

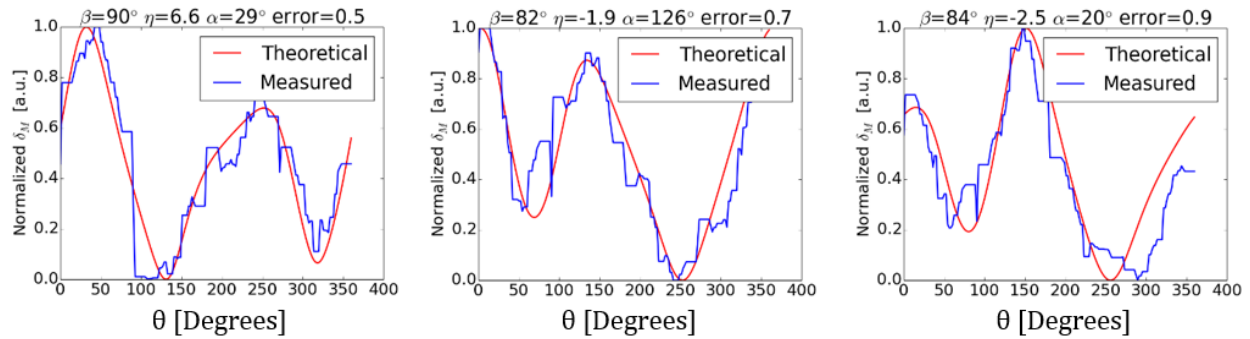


Figure 4.2 Each plot compares the normalized measured $\delta_M^{(loc)}$ profile to the best matching $\delta_M^{(loc)}$ profile of a theoretical crack tip with crack plane orientation (α) and bulk biaxial stress ratio (η) listed in the title, where the bulk first principal stress direction ($\beta_{(\infty)}^{(1)}$) is a known, measured value.

The SVC is trained by a set of δ profiles consisting of 500 bowties and 650 non-bowties that have been manually identified from wafers not included in the set of 18 wafers evaluated here. Each δ profile consists of a list of 100 retardation values where each value in the list is an attribute of the δ profile. When training the SVC, each δ profile is considered to be a 100-dimensional vector and a kernel is used to map each delta profile point so that the clusters of bowtie and non-bowtie points are distinctly separate from

each other and a hyperplane can be placed between them. All future δ profiles can then be classified as bowtie or non-bowtie depending on which side of the hyperplane they reside.

A set of 224 manually identified bowtie and non-bowtie features, separate from the training set, are used to test the accuracy of the SVC and determine the optimal combination of kernel method, regularization parameter, and gamma parameter. The regularization parameter dictates how much error is allowed when placing the hyperplane between the two classes of data points. A large regularization parameter allows for very little error and focuses on classifying all of the data points correctly whereas a small regularization parameter allows for a larger margin of error and produces a less complex hyperplane that may misclassify a larger portion of the training data points. The gamma parameter decides which data points are considered when forming the hyperplane. A large gamma value only takes into consideration points nearest to the plane while a small gamma value considers points both close and far from the plane.

To optimize the SVC, 504 classifiers were tested for accuracy, each classifier consisting of a different combination of kernel method, regularization parameter, and gamma parameter. The optimal combination achieved 93% accuracy, used a radial basis function kernel, a gamma value of 0.0001, and a regularization parameter of 100, where larger regularization parameter values yielded equally accurate results.

Using the SVC to classify a single bowtie is relatively computationally efficient, but classifying every pixel in each image would be prohibitively costly. To reduce computation time, instead of checking every pixel in each image we divide each δ field image into 16 sub-regions and only the location of maximum retardation in each sub-region is checked for a bowtie. Figure 4.3 shows an example of bowties that have been identified in a 5x image of an as-cut wafer that was divided into 64 sub-regions.

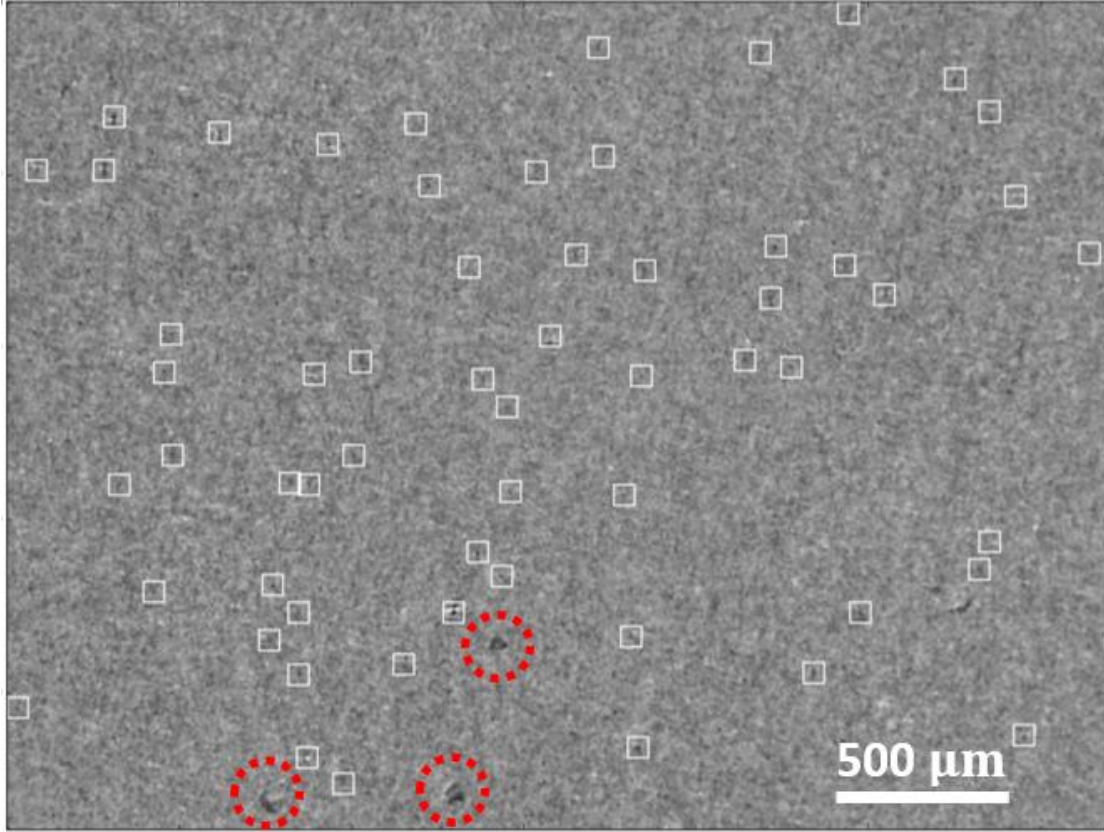


Figure 4.3 Microscopic δ_0 image of an as-cut monocrystalline silicon wafer. Bowties that have been identified by the support vector classifier are boxed. Circled dark features are dust particles that had settled on the wafer surface.

For every bowtie that is identified by the SVC, we record the $\delta_M^{(loc)}$ profile where the δ_M field is calculated according to Eq. (3.13) using the measured δ_0 and δ_{45} fields. We also record the bulk first principal stress direction ($\beta_{(\infty)}^{(1)}$) and the magnitude of $\delta_M^{(\infty)}$. As described in chapter 5, the measured profile of $\delta_M^{(loc)}$ is compared to the calculated $\delta_M^{(loc)}$ profile of a hypothetical crack acted on by a residual stress field with first principal stress direction $\beta_{(\infty)}^{(1)}$. As shown in Fig. 5.2, each microcrack is characterized according to the combination of crack plane orientation (α) and bulk biaxial stress ratio (η) that produce the $\delta_M^{(loc)}$ profile that best matches the measured bowtie pattern.

Chapter 5 – Characterization of microcracks

The bowtie stress field pattern is not unique to the crack tip stress field [32, 37]. In this chapter we will calculate the $\delta_M^{(loc)}$ profile of a hypothetical surface crack and compare it to the measured $\delta_M^{(loc)}$ profile of bowties that have been identified by the SVC. Theoretical $\delta_M^{(loc)}$ profiles are calculated for an array of crack plane orientations and bulk biaxial stress ratios. Each bowtie is characterized according to best matching the theoretical $\delta_M^{(loc)}$ profile. The bulk residual stress field acting on each crack induces the locally elevated stress field around the crack tip. By comparing the local and bulk residual shear stress fields, we derive the complete biaxial bulk residual stress field.

5.1 Analysis of surface cracks

Many of the bowtie shaped stress fields are consistent with the stress field of a surface microcrack. Based on SEM observations, there are surface microcracks present in the regions near bowties of interest. From standard linear elastic fracture mechanics, the stress field near the tip of a crack may be described using the mode I and mode II stress intensity factors according to

$$\sigma_{11} = \frac{K_I}{\sqrt{2\pi r}} \cos\left(\frac{\theta}{2}\right) \left(1 - \sin\left(\frac{\theta}{2}\right) \sin\left(\frac{3\theta}{2}\right)\right) - \frac{K_{II}}{\sqrt{2\pi r}} \sin\left(\frac{\theta}{2}\right) \left(2 + \cos\left(\frac{\theta}{2}\right) \cos\left(\frac{3\theta}{2}\right)\right) \quad (5.1)$$

$$\sigma_{22} = \frac{K_I}{\sqrt{2\pi r}} \cos\left(\frac{\theta}{2}\right) \left(1 + \sin\left(\frac{\theta}{2}\right) \sin\left(\frac{3\theta}{2}\right)\right) + \frac{K_{II}}{\sqrt{2\pi r}} \cos\left(\frac{\theta}{2}\right) \sin\left(\frac{\theta}{2}\right) \cos\left(\frac{3\theta}{2}\right) \quad (5.2)$$

$$\sigma_{12} = \frac{K_I}{\sqrt{2\pi r}} \cos\left(\frac{\theta}{2}\right) \sin\left(\frac{\theta}{2}\right) \cos\left(\frac{3\theta}{2}\right) + \frac{K_{II}}{\sqrt{2\pi r}} \cos\left(\frac{\theta}{2}\right) \left(1 - \sin\left(\frac{\theta}{2}\right) \sin\left(\frac{3\theta}{2}\right)\right) \quad (5.3)$$

$$\bar{\sigma} = \begin{bmatrix} \sigma_{11} & \sigma_{12} \\ \sigma_{21} & \sigma_{22} \end{bmatrix} \quad (5.4)$$

where r is the radius from the crack tip, θ is the in-plane angle from the crack tip, and K_I and K_{II} are the mode I and mode II stress intensity factors. For the purpose of this study, the field may be assumed to apply inside a distance at which the locally elevated retardation becomes large relative to the noise in the

measured δ_M image, which is typically around 30 μm . Eq. (5.4) assumes that the crack-plane is orthogonal to the surface and subject to biaxial stress. These are fair assumptions since fractographic analysis suggests that a critical microcrack -- one that will initiate wafer failure -- will be favorably oriented with respect to the externally applied load [12]. An external load such as four line bending or wafer handling will result in a tensile load along one of the wafer's surfaces. Thus a favorably oriented microcrack will be one whose crack plane is normal to both the wafer surface and the applied loading direction.

Rotating $\bar{\sigma}$ by α , the angle between the crack plane and the [100] direction on the wafer, aligns the crack tip stress field coordinate system with the x-y coordinate system of the GFP. We will refer to the rotated stress field as σ . Then, substituting Eq. (5.1-5.3) into Eq. (3.11-3.14) provides the form for the calculated δ_0 , δ_{45} , and δ_M fields shown in Fig. 5.1.

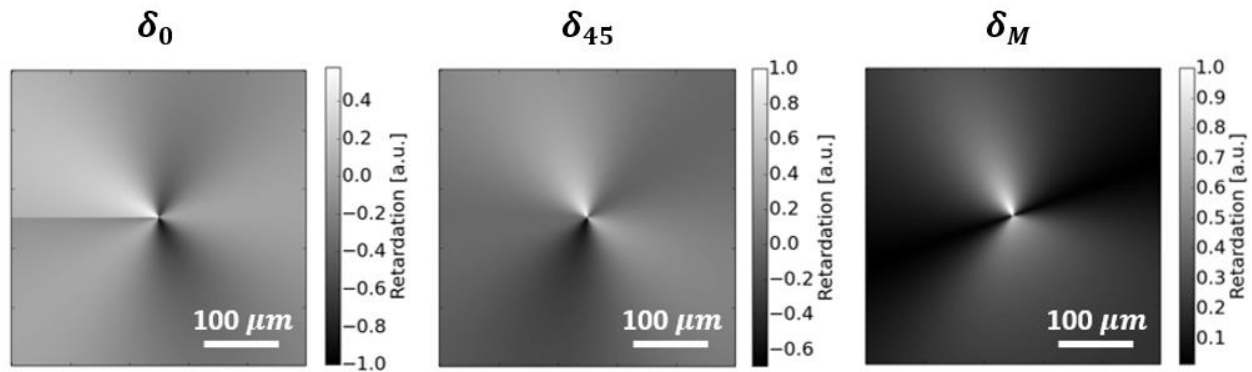


Figure 5.1 Retardation caused by the theoretical stress field near a typical surface crack.

Comparing Fig. 3.3 and Fig. 5.1 it can be seen that the theoretical δ fields for a crack tip closely resemble the bowtie pattern observed in the measured δ fields. Some differences exist between Fig. 3.3 and Fig. 5.1, such as the discontinuity and bowtie size. The theoretical crack tip stress field does not account for body geometry, such as cracks stemming radially from pits in the wafer surface, or for the bulk residual stress field; both contribute to the size and shape of the measured bowtie profile. However, within the region of K dominance, the measured and theoretical bowtie fields closely resemble each other, as shown in Fig. 4.2.

Other locally elevated stress fields, such as those induced by trapped particles, also produce similar patterns. To determine whether a bowtie pattern belongs to a crack tip, we compare the profile around each bowtie to theoretical crack tip retardation fields. Each δ field is composed of a local and bulk component such that

$$\delta = \delta^{(loc)} + \delta^{(\infty)} \quad (5.5)$$

where $\delta^{(loc)}$ is the bowtie pattern component of the δ field caused by the presence of a microcrack and $\delta^{(\infty)}$ is the constant component of the δ field caused by the bulk residual stress field in the wafer.

The δ fields of several thousand surface cracks have been measured over a total of 18 etched PV silicon wafers. Each δ field is analyzed in order to characterize each crack by its stress intensity factors, the geometric factor (χ) that relates applied stress to the stress intensity factors, and the ratio of bulk principal stresses acting on each crack (η). Ultimately $\delta_M^{(\infty)}$ and η will be used to determine the bulk biaxial stress field acting on each crack. Finally, in accordance with weakest link theory, the strength of each wafer is calculated based on the most detrimental surface crack.

5.2 Theoretical local retardation field

Next we characterize the measured $\delta_M^{(loc)}$ profile by comparing it to the $\delta_M^{(loc)}$ profile of a theoretical crack tip stress field. An array of $\eta = \sigma_{(\infty)}^{(1)}/\sigma_{(\infty)}^{(2)}$ and α input values will be used to check which combination produces the best match between the theoretical and measured $\delta_M^{(loc)}$ profiles. The local retardation field is derived for a surface crack as a function of α , $\beta_{(\infty)}^{(1)}$, $\beta_{(loc)}^{(1)}$, wafer thickness t , angle between the location on the crack front and wafer surface ϕ , in-plane radius from crack tip ρ , and the ratio of bulk residual principal stresses η .

We start by substituting σ , the crack tip stress field rotated by α , into Eq. (3.11-3.14), giving

$$\delta_M^{(loc)} = \frac{C(\beta_{(loc)}^{(1)})}{2\sqrt{\pi\rho}} t {}_2F_1\left(\frac{1}{4}, \frac{1}{2}; \frac{3}{2}; -\frac{t^2}{\rho^2}\right) \sqrt{K_I^2(1 - \cos(2\theta)) + 4K_I K_{II} \sin(2\theta) + K_{II}^2(1 + 3 \cos(2\theta))} \quad (5.6)$$

where $C(\beta_{(loc)}^{(1)})$ is the stress optic coefficient along the local first principal stress direction and ${}_2F_1(a_1, a_2; b_1; -t^2/\rho^2)$ is Gauss's hypergeometric function. Equation (5.6) can be rewritten in terms of the ratio of stress intensity factors, so that

$$K_R = K_I/K_{II} \quad (5.7)$$

$$\delta_M^{(loc)} = \frac{C(\beta_{(loc)}^{(1)})}{2\sqrt{\pi\rho}} t {}_2F_1\left(\frac{1}{4}, \frac{1}{2}; \frac{3}{2}; -\frac{t^2}{\rho^2}\right) |K_{II}| \sqrt{K_R^2(1 - \cos(2\theta)) + 4K_R \sin(2\theta) + 3 \cos(2\theta) + 1} \quad (5.8)$$

The stress intensity factors are the product of a geometric factor and the bulk stress field acting on a crack [38, 39], or

$$K_i = \sigma_i^{(\infty)} \chi \quad (5.9)$$

$$\sigma_I^{(\infty)} = \sigma_{(\infty)}^{(2)} (\cos^2(\beta_{(\infty)}^{(2)} - \alpha) + \eta \sin^2(\beta_{(\infty)}^{(2)} - \alpha)) \quad (5.10)$$

$$\sigma_{II}^{(\infty)} = \sigma_{(\infty)}^{(2)} (1 - \eta) \cos(\beta_{(\infty)}^{(2)} - \alpha) \sin(\beta_{(\infty)}^{(2)} - \alpha) \cos(\phi) \quad (5.11)$$

$$K_R = \frac{\cos^2(\beta_{(\infty)}^{(2)} - \alpha) + \eta \sin^2(\beta_{(\infty)}^{(2)} - \alpha)}{(1 - \eta) \cos(\beta_{(\infty)}^{(2)} - \alpha) \sin(\beta_{(\infty)}^{(2)} - \alpha) \cos(\phi)} \quad (5.12)$$

where χ replaces $\sqrt{\pi l}$ where l is a function of crack geometry. We consider χ to be a constant property of each microcrack. Since the exact shape of each crack is unknown but the entire crack front contributes to the measured $\delta_M^{(loc)}$ field, an average value for $\cos(\phi)$ of $2/\pi$ is assumed. Furthermore, it is the profile and not the magnitude of $\delta_M^{(loc)}$ that is used to determine α and η , thus $\delta_M^{(loc)}$ is normalized by all axisymmetric components. Then $\delta_M^{(loc)}$ can be written in terms of all axisymmetric components or, equivalently, in terms of all θ dependent components, such that

$$\delta_{M-Norm}^{(loc)} = -\frac{2\sqrt{\pi\rho} \delta_M^{(loc)}}{(\sigma_{(\infty)}^{(1)} - \sigma_{(\infty)}^{(2)}) \chi t {}_2F_1\left(\frac{1}{4}, \frac{1}{2}; \frac{3}{2}; -\frac{t^2}{\rho^2}\right)} \quad (5.13)$$

$$\delta_{M-Norm}^{(loc)} = C(\beta_{(loc)}^{(1)}) \sqrt{4(1 - \eta) \left(\sin^2(\alpha - \beta_{(\infty)}^{(1)}) + \eta \cos^2(\alpha - \beta_{(\infty)}^{(1)}) \right)^2 (1 - \cos(2\theta)) + \left((1 - \eta) \cos(\alpha - \beta_{(\infty)}^{(1)}) \sin(\alpha - \beta_{(\infty)}^{(1)}) \cos(\phi) \sin(2\theta) \right)^2 + \left((1 - \eta) \cos(\alpha - \beta_{(\infty)}^{(1)}) \sin(\alpha - \beta_{(\infty)}^{(1)}) \cos(\phi) \right)^2 (5 + 3 \cos(2\theta))} \quad (5.14)$$

Note that $\delta_{M-Norm}^{(loc)}$ depends on both the bulk and local first principal stress directions. The local first principal stress direction can be rewritten in terms of K_R , α , $\beta_{(loc)}^{(1)}$, and θ and expressed as

$$\beta_{(loc)}^{(1)} = \arctan \left(\frac{K_R \left(\cos \left(2\alpha + \frac{\theta}{2} \right) - \cos \left(2\alpha + \frac{5}{2}\theta \right) \right) + \sin \left(2\alpha + \frac{5}{2}\theta \right) + 3 \sin \left(2\alpha + \frac{\theta}{2} \right) + \sqrt{2K_R^2 (1 - \cos(2\theta)) + 8K_R \sin(2\theta) + 6 \cos(2\theta) + 10} \frac{\sin(2\beta_{(\infty)}^{(1)} - 2\alpha)}{\sin(2\beta_{(\infty)}^{(1)} - 2\alpha)}}{K_R \left(\sin \left(2\alpha + \frac{5}{2}\theta \right) - \sin \left(2\alpha + \frac{\theta}{2} \right) \right) + 3 \cos \left(2\alpha + \frac{\theta}{2} \right) + \cos \left(2\alpha + \frac{5}{2}\theta \right)} \right) \quad (5.15)$$

Values for α and η when inserted into Eq. (5.14) provide profiles of $\delta_{M-Norm}^{(loc)}$ for a variety of crack orientations and bulk residual principal stress ratios. Each profile is calculated for θ ranging from 0 to 2π and then scaled to range from 0 to 1. As shown in Fig. 6.2, computed profiles are compared to measured profiles for individual bowtie patterns.

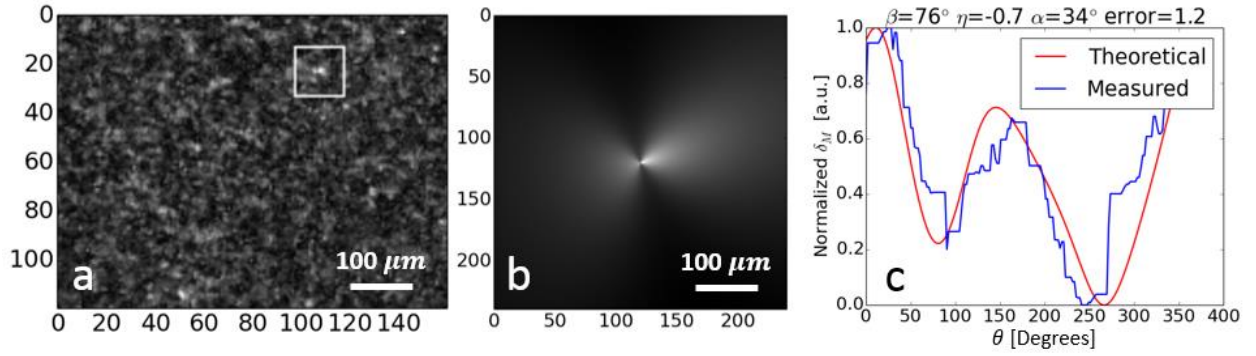


Figure 5.2 The $\delta_M^{(loc)}$ profile of a measured bowtie (a) is compared to the best matching profile of a theoretical bowtie (b). Every profile consists of the average values of a 20 μm radius line scan swept in a full circle around a bowtie. The observed difference in bowtie size is because in (a), when more than 30 μm from the crack tip, the local retardation becomes small compared to the bulk retardation and system noise while in (b) there is no bulk retardation or noise.

Each microcrack is characterized by the combination of α and η that correspond to the normalized theoretical $\delta_M^{(loc)}$ profile that best matches the normalized measured $\delta_M^{(loc)}$ profile. The best matching profile is determined by the method of least squares. Only bowties which fit the profile of a crack tip retardation field whose plane is normal to the wafer surface are accepted as crack tip stress fields. This helps to prevent misidentification of artifacts, such as dust particles, which appear to be locally elevated stress fields, as microcracks. Furthermore, the population of bowtie profiles accepted as microcracks by this method will consist of cracks whose planes are approximately orthogonal to the wafer surface. While

the identification of oblique cracks is excluded in this work, this method may be adapted to identify oblique cracks as well by also considering theoretical $\delta_M^{(loc)}$ profiles for oblique cracks when characterizing each bowtie.

Once α and η have been determined by the above process, the ratio of stress intensity factors (K_R) can be calculated from Eq. (5.12). Then Eq. (5.8), when set equal to the measured $\delta_M^{(loc)}$ at a known location (ρ, θ) , can be used to solve for the mode II stress intensity factor. Finally, using Eq. (5.7), the mode I stress intensity factor is obtained.

5.3 Calculating the biaxial stress state near microcracks

Having determined η acting on each microcrack, we can calculate the complete biaxial bulk residual stress field by solving the system of equations $\eta = \sigma_{(\infty)}^{(1)}/\sigma_{(\infty)}^{(2)}$ and $\Delta\sigma_{(\infty)} = \sigma_{(\infty)}^{(1)} - \sigma_{(\infty)}^{(2)}$ which gives

$$\sigma_{(\infty)}^{(1)} = \frac{\eta\Delta\sigma_{(\infty)}}{1 - \eta} \quad (5.16)$$

$$\sigma_{(\infty)}^{(2)} = \frac{\Delta\sigma_{(\infty)}}{1 - \eta} \quad (5.17)$$

$$\sigma_{(\infty)}^{\perp} = \sigma_{(\infty)}^{(1)} \sin^2(\alpha - \beta_{(\infty)}^{(1)}) + \sigma_{(\infty)}^{(2)} \cos^2(\alpha - \beta_{(\infty)}^{(1)}) \quad (5.18)$$

where $\sigma_{(\infty)}^{\perp}$ is the normal component of the bulk residual stress acting on the microcrack. The full wafer measured bulk difference in principal stress field ($\Delta\sigma_{(\infty)}$), shown below, has been reconstructed from the average $\delta_M^{(\infty)}$ values of 3,500 IR-GFP images taken of etched Czochralski grown silicon wafers while using the 5x objective.

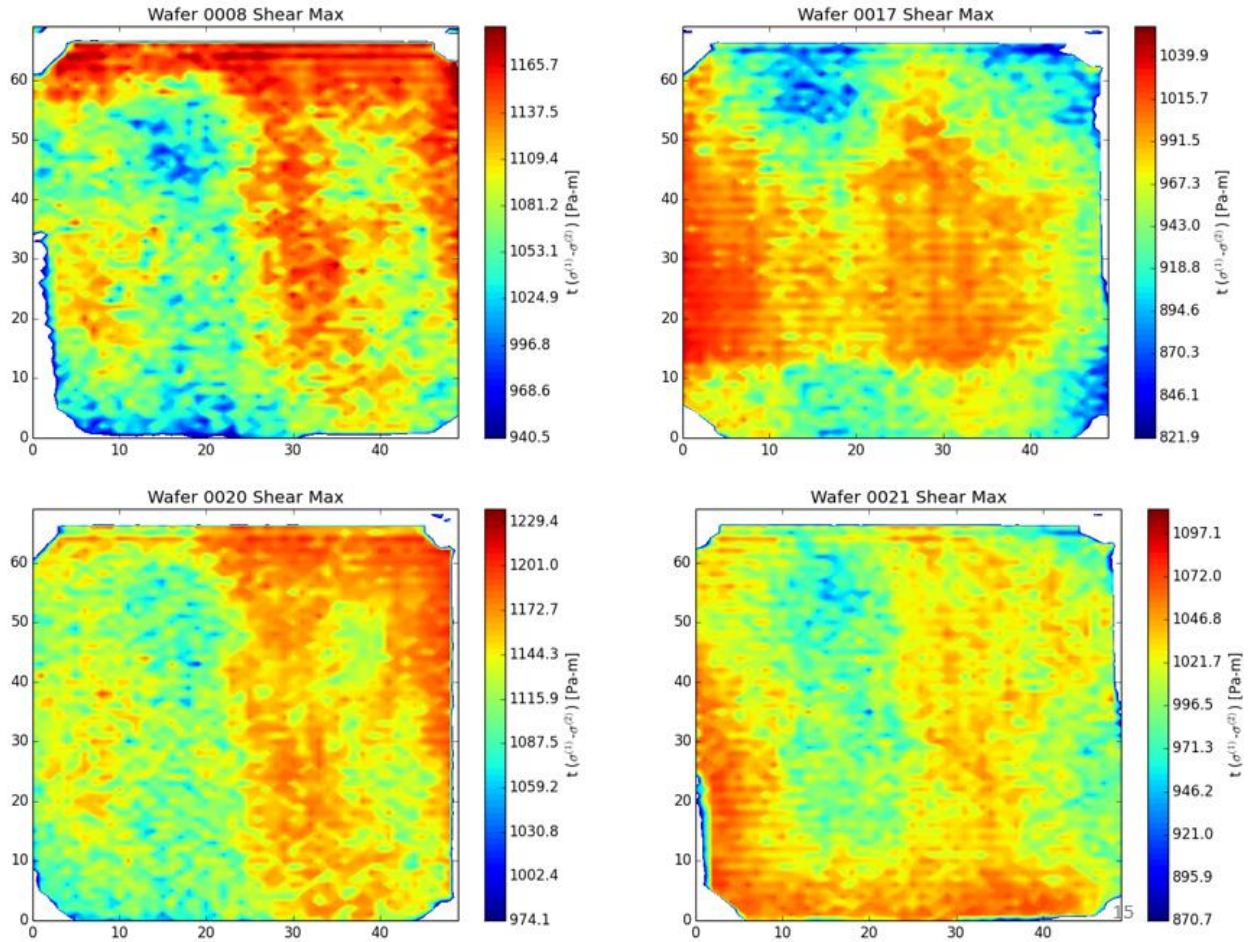


Figure 5.3 Difference in principal stress field for 4 etched (100) Cz-Si wafers that are 176 μm thick. Axial direction of wire saw is vertical in each image and odd numbered wafers are rotated 180 degrees from even numbered wafers. The wafers shown here are typical samples from the batch of wafers evaluated in this study. The horizontal striation pattern is a result of the raster scan imaging process.

Measurements are in stress \cdot thickness, and can be converted to stress by dividing by the thickness over which the retardation accumulates. The horizontal line features are a result of the raster scanning method used to collect 5x images. Elevated or low values along the immediate edge of the wafer may result from the light source reflecting off of the internal edge of the wafer at or near Brewster's angle, thus altering the polarization. While the shape of the measured difference in principal stress field is consistent from wafer to wafer it is not consistent with the theoretical thermal residual stress field that might be expected to arise in a wafer cut from a 200 mm diameter Czochralski grown ingot [22, 40]. It is possible that the

asymmetry observed in the difference in principal stress fields is a result of uneven cooling while the silicon ingot solidified resulting in a thermal gradient across the ingot. Notice also that the measured magnitude of difference in principal stresses varies by only about twenty percent from minimum to maximum across each wafer indicating that the background stress is actually relatively uniform. We speculate that the magnitude of the difference in principal stress field is potentially the result of two factors. First, while the illumination source is a narrow-band light source centered at 1150 nm, it is not monochromatic, and thus cannot be perfectly circularly polarized. Any deviation from circular polarization will appear as retardation in the measured data. Prior to imaging, a stress-free electronic grade wafer is measured to check how circularly polarized the light source is. A stack of waveplates is then adjusted to form a quarter waveplate to ensure the light source is as close to circularly polarized as possible. The second factor is the presence of the saw damage layers. The theoretical stress fields inferred in [22] only account for thermal residual stresses and dislocation stress fields. It is possible that the elevated difference in principal stresses observed in Fig. 5 are the result of a combination of thermal residual stresses and damage induced by the wafer slicing process. Popovich et al. [27] used micro-Raman spectroscopy to measure residual stress in the saw damage layer of multicrystalline silicon wafers and under the assumption of a biaxial stress state found the stresses to be approximately 500 MPa.

In considering the stress due to the saw damage, we assume that $\delta_M^{(\infty)}$ accumulates at a constant rate over the saw damage layers on the top and bottom surface of the wafer, each with a thickness of t_{sd} . This assumption allows for the simplification of Eq. (5.16) and Eq. (5.17), so that

$$\sigma_{(\infty)}^{(1)} = \frac{\eta \delta_M^{(\infty)}}{(1 - \eta) t_{sd} \mathcal{C}(\beta_{(\infty)}^{(1)})} \quad (5.19)$$

$$\sigma_{(\infty)}^{(2)} = \frac{\delta_M^{(\infty)}}{(1 - \eta) t_{sd} \mathcal{C}(\beta_{(\infty)}^{(1)})} \quad (5.20)$$

where the calculated bulk stress acting on each crack shares an inverse relationship with the assumed saw damage layer thickness. The saw damage layer on LAWS wafers is generally between 25 and 40 μm in

depth [16], approximately 13 μm of which were removed from each surface of the wafers used in this study. Thus the results have been calculated assuming the saw damage layer is 12 μm thick. Results are also provided for saw damage layer thicknesses of 7 and 17 μm to show how this assumption affects the calculated Weibull parameters.

5.4 Crack Geometric Factor

Having determined the mode I stress intensity factor of each crack and the normal component of the bulk residual stress acting on each crack, we make the assumption that the relationship between K_I and $\sigma_{\perp}^{(\infty)}$ remains linear until the crack geometry changes upon crack propagation. We refer to this relationship as the crack geometric factor, χ .

Chapter 6 – Characterization of wafer strength

6.1 Weibull statistics

The distribution in size, density, and orientation of microcracks results in a spread of wafer strengths. Weibull noted that this is true for all materials and that while a definite strength does not exist, the mean strength and dispersion of strengths can be used to determine the probability of failure at a given applied tensile load [41]. Thus, for a system whose survival depends on the survival of all of its volume elements, such as a series of uniform bars under tension or a brittle plate like the silicon wafer considered here, the probability of the system surviving an applied load can be determined by multiplying the probabilities of each volume element surviving [41]

$$P_S = p_s^{(1)} p_s^{(2)} \dots p_s^{(N)} \quad (6.1)$$

The probability of survival of the i^{th} volume element is represented by $p_s^{(i)}$ and the probability of survival of the system is represented by P_S . This statistical approach to predicting the probability of survival is known as the weakest link theory. Each volume element can be thought of as a link in a chain and when the weakest link breaks, the system will fail. This approach applies well to silicon wafers since failure can be assumed to occur when the first crack begins to propagate under tension [42].

The probability of failure of any given wafer is the complement of P_S and is given by

$$P_F(\sigma) = 1 - \exp \left[- \left(\frac{\sigma^{(i)} - \lambda}{\sigma_\theta - \lambda} \right)^b \right] \quad (6.2)$$

where the location parameter λ , which may be zero, represents the lowest $\sigma^{(i)}$ at which failure may occur. The characteristic fracture strength σ_θ is the value at which the probability of a sample failing is 63.2%. The value 63.2% arises from Eq. (6.2), since when σ equals σ_θ the probability of failure reduces to $1 - e^{-1}$. The shape parameter b is a measure of the scatter of $\sigma^{(i)}$ values at which samples fail. Large shape parameter values represent low dispersion which is the case for materials with small variations in strength, such as steel [42]. In contrast, brittle materials such as silicon have a large spread in failure

strengths and thus, small shape parameter values, because their failure is dependent on the probability of encountering a critical flaw.

Conventionally, the Weibull parameters in this case would be experimentally determined by fracturing a set of wafers under a uniform applied load and calculating the stress at which each wafer failed. Since uniform tensile loads are difficult to apply to a brittle wafer without failure resulting from the gripping mechanism, fracture tests may alternatively be done via four-line bend test or ring on ring test [3, 21, 22]. The Weibull parameters can then be determined by assigning a probability of failure to each wafer according to the order in which they failed such that

$$P_F = \frac{n - 0.3}{N + 0.4} \quad (6.3)$$

where P_F is the assigned probability of failure. N is the total number of wafers and n is the order in which a given wafer failed ranging from 1 to N . Equation (6.3) is used in conventional Weibull analysis [5, 43]. The values 0.3 and 0.4 are from the approximate median rank estimate, which if omitted, results in an overestimate of the probability of failure. Plotting $\ln | - \ln |1 - P_F||$ versus $\ln |\sigma - \lambda|$ and finding the best fit line reveals the shape parameter as the slope and the characteristic strength as the x-intercept. The location parameter can be found by maximizing the coefficient of determination, R^2 [43]. When the location parameter is zero the Weibull distribution is sufficiently described by two parameters instead of three. When inserted into the Weibull distribution, these parameters are used to predict the probability of failure of a randomly selected wafer at a given applied load.

We base the survival of each volume element, an 800 by 600 μm rectangular region, on the bowtie feature with the greatest $\delta^{(loc)}$ value. Volume elements that contain a bowtie feature caused by a microcrack are characterized by the uniaxial tensile stress required to increase the mode I stress intensity factor of the crack to equal the fracture toughness of silicon. Thus, when the mode I stress intensity factor equals the fracture toughness of silicon, the probability of survival of the volume element is zero.

6.2 Calculated wafer strength

Due to the brittle nature of silicon, as soon as any crack begins to propagate under tension, the wafer is assumed to fail. Thus the strength of each wafer is characterized by the applied tensile load which results in the mode I stress intensity factor of any crack surpassing the fracture toughness of silicon. Like the stress-optic coefficient, the fracture toughness of (100) silicon is also anisotropic and depends on the orientation of the crack plane [44]. The critical applied uniaxial tensile stress and fracture toughness are related by

$$K_{IC}^{(\alpha)} = \chi \left(\sigma_{\perp}^{(\infty)} + \sigma_C^{(appl)} \sin^2(\alpha - \psi) \right) \quad (6.4)$$

where $K_{IC}^{(\alpha)}$ is the mode I fracture toughness of silicon for a crack whose plane is oriented along α , $\sigma_C^{(appl)}$ is the critical applied tensile load that results in crack propagation, and ψ is the in-plane angle from the [100] direction along which $\sigma^{(appl)}$ is applied. We use experimentally determined fracture toughness values for (100) silicon, $K_{IC}^{[110]}$ and $K_{IC}^{[100]}$ of $1.21 \text{ MPa}\sqrt{\text{m}}$ and $1.97 \text{ MPa}\sqrt{\text{m}}$, where [110] and [100] are the direction of normal stress acting on the surface crack [44]. We calculate the fracture toughness according to

$$K_{IC}^{(\alpha)} = \left(\left(\frac{\sin(2\alpha)}{K_{IC}^{[110]}} \right)^2 + \left(\frac{\cos(2\alpha)}{K_{IC}^{[100]}} \right)^2 \right)^{-\frac{1}{2}} \quad (6.5)$$

The form of Eq. (6.5) was selected to satisfy the fracture toughness values presented by Li et al. and to mimic the anisotropic behavior observed in the (100) silicon stress optic coefficient and elastic modulus [44]. Using Eq. (6.4), $\sigma_C^{(appl)}$ is calculated for all of the analyzed microcracks and the lowest value is used to characterize the strength of each wafer. Finally, according to the methods described in section 6.1 the Weibull parameters for the batch of wafers are calculated from the set of calculated wafer strengths.

6.3 Results and discussion

Figure 6.1 shows the distribution of wafer strengths, as calculated by the methods described above, on a Weibull plot. The Weibull parameters portrayed in Fig. 6.1 are dependent on ψ , the direction of the applied uniaxial tensile load.

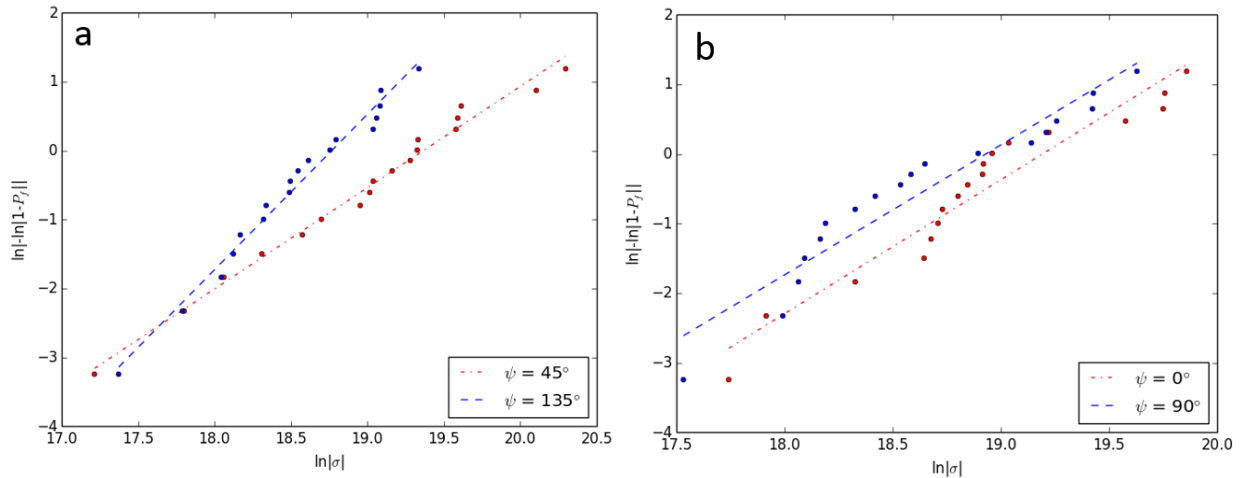


Figure 6.1 Weibull plot of wafer strengths for a uniaxial tensile load applied along ψ . The difference in strength observed in (a) likely stems from the distribution of flaw orientations which shows that a larger portion of flaws are approximately orthogonal to $\psi = 135^\circ$. The difference in strength observed in (b) may result from the direction of first principal stress in the saw damage layer. The magnitude of compressive residual stress is less along $\psi = 90^\circ$ resulting in a lower applied stress required to initiate failure.

Figure 6.2 shows how the characteristic strength and Weibull shape parameter of the wafer batch vary with the direction of applied uniaxial tension for three assumed saw damage layer thicknesses.

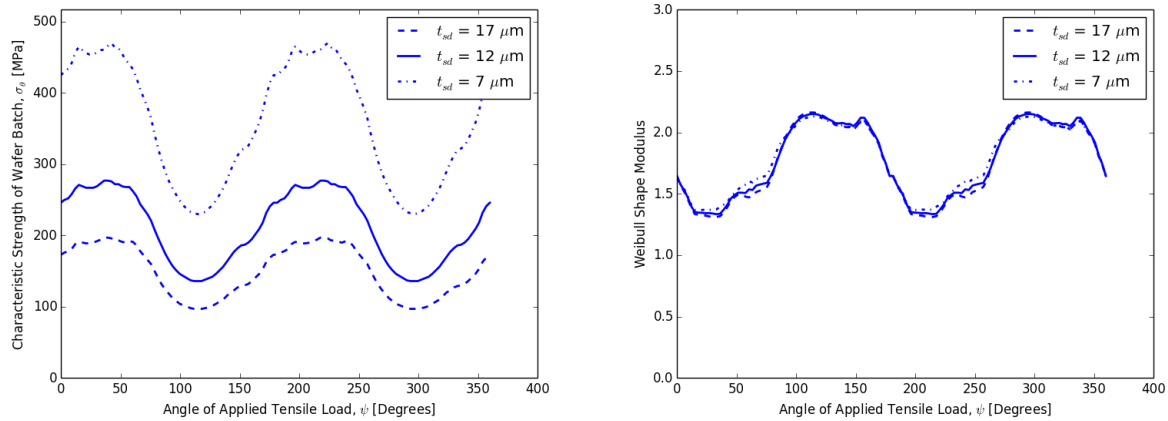


Figure 6.2 Dependence of the characteristic strength and Weibull shape parameter on the direction of applied loading for a range of assumed saw damage layer thicknesses.

The characteristic strength of the wafer batch is greater when the wafer is loaded perpendicular to the direction of wire motion than when loaded parallel to the direction of wire motion. The direction of wire and ingot motion are respectively along $\psi = 90^\circ$ and $\psi = 0^\circ$. As shown in Table 1, this variation in wafer fracture strengths has been observed in both slurry and diamond wire sawn multicrystalline silicon wafers [17].

Table 1 Weibull parameters for wafers loaded parallel and perpendicular to the direction of wire motion; lines with bold text indicate data from this study.

*Values interpreted from Weibull plots

Wafer Type and Condition	Wire Sawing Process	Load Configuration	Orientation	σ_θ [MPa]	Weibull modulus
c-Si etched	Slurry Cut	Pure Tension	 	166	1.9
c-Si etched	Slurry Cut		⊥	216	1.6
virtual c-Si [9]	-		-	109	2.5
mc-Si etched [45]	Diamond Cut	Four Line Bending		165	7.6*
mc-Si etched [45]	Diamond Cut		⊥	292	9.2*
qc-Si etched [45]	Diamond Cut			181	7.0*
qc-Si etched [45]	Diamond Cut		⊥	343	7.1*
mc-Si as cut [17]	Slurry Cut			141	8.4
mc-Si as cut [17]	Slurry Cut		⊥	157	7.7
mc-Si as cut [46]	Slurry Cut			144	22.1
mc-Si as cut [46]	Slurry Cut		⊥	146	13.1

The characteristic strength of wafers loaded perpendicular to the wire saw direction has been observed to be 88 (11) percent greater than wafers loaded parallel to the wire saw direction for diamond (slurry) sawed wafers [17]. The set of wafers studied here has a characteristic strength which is 30 percent greater when loaded perpendicular to the direction of wire motion than when loaded parallel to the direction of wire motion. In the same study [17], the authors also observed increased Weibull shape modulus when loading the samples parallel to the saw damage, suggesting less scatter in the set of wafer strengths. This is also observed in our calculated shape parameter values shown in Fig. 7. When loaded perpendicular (parallel) to the wire saw direction the shape modulus is 1.6 (1.9).

The variance in characteristic strength and Weibull shape parameter appears to originate from the observed distribution of crack orientations and preferential first bulk residual principal stress direction shown in Fig. 6.3.

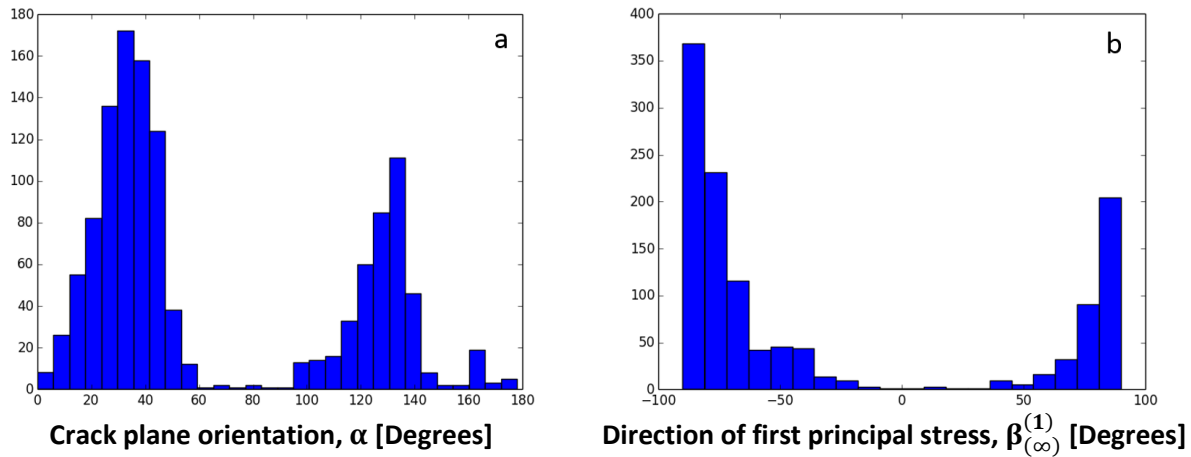


Figure 6.3 (a) Histogram of crack plane orientations. Population shown consists of microcracks that match the theoretical $\delta_M^{(loc)}$ profile with the least amount of error. (b) Histogram of direction of the bulk first principal stress from a typical wafer.

All of the microcracks represented in Fig. 6.3a are believed to be approximately orthogonal to the wafer surface. This is because Eq. (5.6-5.15) for theoretical $\delta_M^{(loc)}$ assume the crack is orthogonal to the surface. Thus when the theoretical and measured $\delta_M^{(loc)}$ profiles are compared to determine α and η , cracks that are orthogonal to the surface are the best match to the theoretical profile. Furthermore, using the

detection methods outlined in chapter 4, oblique cracks are less likely to be detected when identifying bowties since they result in lower in-plane shear stress. At first glance, the clear bimodal distribution suggests that cracks oriented orthogonal to the surface typically lie along directions 35° and 135° from the [100] direction. However, the crack detection methods used here influence the observed bimodal distribution of crack plane orientations. This is because in each observed region we analyze the crack exhibiting the greatest local retardation, which, as seen in Eq. (18), is proportional to the magnitude of the stress intensity factors of the crack. The stress intensity factors depend on the crack geometry and the orientation of the crack with respect to the principal bulk residual stresses acting on the crack. Cracks oriented along the first or second bulk principal stress direction have a mode II stress intensity factor that is equal to zero. Since the residual stresses in the saw damage layer are compressive in nature [16, 27], the mode II stress intensity factor has a strong effect on the magnitude of local retardation. Thus this method of crack detection is biased towards identifying cracks that are oriented skew to either bulk principal stress direction. As shown in Fig. 6.3b, the most common first bulk principal stress direction is along the direction of wire motion. Therefore with this method, the likelihood of characterizing a crack whose plane is oriented skew to the direction of wire motion is greater than that of a crack whose plane is parallel or perpendicular to the direction of wire motion. This bias is likely responsible for the large variation in wafer strength with respect to loading direction as observed in Fig. 6.2a and the similarity of Weibull moduli observed in 6.1b.

Weibull moduli depend on the loading conditions used to fracture each wafer. The greater the area loaded in tension, the greater the probability of encountering a critical flaw; four line bending tests, for example, yield lower characteristic strengths than ring on ring tests, though this is also related to the introduction of additional failure modes along the edge or corners of the wafers [47]. In this work the uniaxial tensile load used to characterize each wafer's strength was in part selected because of its uniformity across the entire wafer, and because we do not know which surface each crack resides on.

Under a uniaxial tensile load a crack on the top or bottom surface of the wafer will experience the same applied stress. Furthermore, unlike four line bending where only a fraction of one surface is in tension, uniaxial tension stresses the entire top and bottom surface thus greatly increasing the number of active surface cracks that may initiate wafer failure.

The Weibull parameters provided in this section are for a group of wafers fractured under a uniaxial tensile load. However, using the measured density of cracks and distribution of crack geometric factors shown in Fig. 6.4 we can estimate the Weibull parameters for the same wafers subjected to four-line bending.

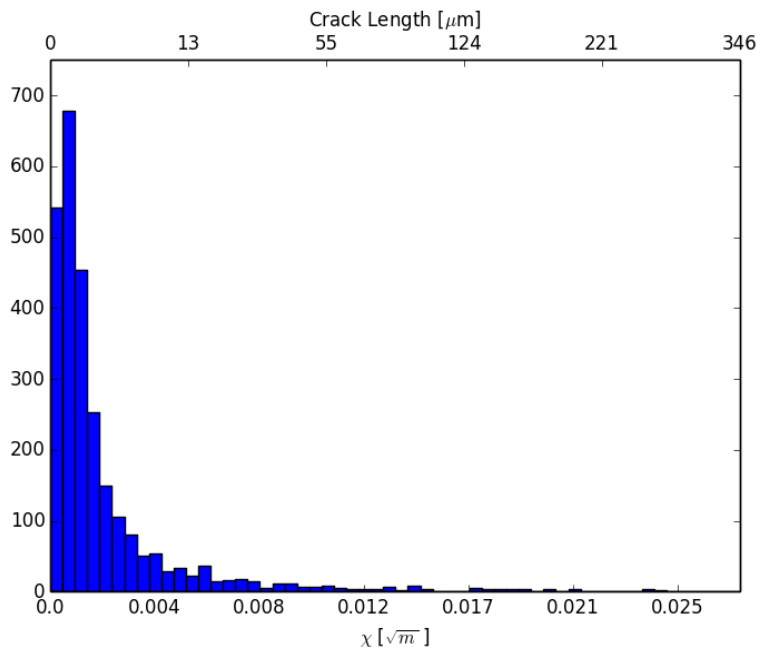


Figure 6.4 Distribution of crack geometric factors for the microcracks used to characterize the strength of each wafer. The secondary x axis represents the microcrack length assuming the crack is semicircular in shape. The geometric factors were calculated under the assumption that $t_{sd} = 12\mu\text{m}$.

Using this distribution of flaws we can calculate the expected difference in characteristic strength for a group of wafers loaded by uniaxial tension and by four-line bending. The distribution of microcracks is typically higher near the edges than near the centers of the wafers [5], but for simplicity we assume the

distribution to be uniform across the wafer. We assume that each crack is orthogonal to the wafer surface, that the in-plane orientation is random, and that each crack is equally likely to be located on the top or bottom surface of the wafer. One thousand virtual wafers with crack distributions based on Figure 6.4 are fractured by applying tensile and four-line bending loads. The expected characteristic strength for wafers fractured by four-line bending is 80% greater than for uniaxial tension, while the shape modulus is 39% lower for four-line bending than for uniaxial tension.

Chapter 7 – Conclusions and future work

7.1 Concluding statements

In this work, etched Czochralski grown silicon PV wafers are inspected with a high resolution IR-GFP in order to observe microscopic surface crack stress fields. A machine learning algorithm was used to identify surface crack stress fields which were then compared to the ideal crack tip stress fields in order to characterize each crack according to the crack plane orientation and ratio of bulk principal stresses acting on the crack. The direction of first principal stress, ratio of bulk principal stresses, and difference in bulk principal stresses were used to determine the biaxial stress state acting on each crack. The stress intensity factors for each flaw were calculated according to the bulk stress acting on the crack, the crack orientation, and the measured local retardation field. The crack geometric factor was derived from the bulk residual stress acting on each crack and the stress intensity factor for each crack. The distribution of crack geometric factors and crack orientations was then used to calculate the strength of each wafer under a virtual uniaxial tensile load. Finally the distribution of wafer strengths was used to calculate the Weibull parameters for the group of wafers.

This approach uses two new methods to allow us to nondestructively characterize individual silicon wafers according to strength, evaluate the Weibull parameters for the wafer group, and solve for the complete biaxial residual stress field in the vicinity of microcracks. The first method involves the identification and classification of microcracks in PE materials via machine learning, PE measurements, and the theoretical crack tip stress field. While this method is not limited to silicon wafers and may also find usefulness in applications for glass characterization, the method is limited by the spatial resolution of the polariscope and by the assumption of the location of each microcrack. In this work a 5x objective was added to the optical path to obtain sufficient resolution to study the profile of the retardation fields around crack tips. This comes at the cost of a reduced field of view and thus increased wafer imaging times. As for the crack location assumption, due to the nature of the distribution of microcracks in silicon wafers we assumed that all observed flaws are surface flaws. This assumption is supported by the

substantial reduction in bowtie density observed from as-cut to etched wafers. This assumption will not necessarily apply to applications where cracks are not primarily due to saw damage.

The second method presented here is the use of a virtual uniaxial tensile load to calculate the strength of each wafer and utilize the spread of strengths to determine the wafer group's Weibull parameters. This method can also be expanded on by replacing the applied uniaxial tensile stress with a known stress distribution, such as that of a Bernoulli gripper [48].

This will allow for wafer strength calculations to be done for each loading condition a wafer will experience during the fabrication process, as well as provide Weibull parameters that are specific to each stage of the cell fabrication process. The use of a virtual uniaxial load is beneficial because it engages all of the surface flaws on both sides of the wafer equally thus providing a better estimate of the strength of each wafer than would be obtained from a bending load that only engages a fraction of the flaws on one surface. This also circumvents the obstacle of not knowing which surface a flaw resides on.

Limitations to the methods presented include the inability to characterize cracks that reside within several millimeters of the edge of the wafer and that microcracks with relatively small stress intensity factors will be overlooked. The former is due to an additional change in polarization caused by reflections off of the internal edge of the wafer at or near Brewster's angle. The latter is a result of only characterizing the bowtie with the greatest local retardation; thus cracks with lower stress intensity factors are ignored when a more critical crack is present in the same region. This gives rise to the bimodal distribution of observed crack plane orientations and is problematic because in a given region, the crack with the greatest stress intensity factors under the residual stress of the wafer will not necessarily be the crack with the greatest stress intensity factor under an external load.

The wafer strengths calculated using this approach are in relative agreement with published wafer strengths for etched monocrystalline silicon wafers [10, 13, 30-32]. In future applications of the methods

described here, a more definitive estimate of the saw damage layer thickness and how the thickness varies across each wafer will increase the accuracy of characteristic strength calculations.

7.2 Future improvements

The advantages of the methods described in this thesis lie in the ability to nondestructively characterize wafers according to the defects responsible for wafer failure and the thoroughness of accounting for nearly every location on both surfaces of the wafer. However, these strengths are accompanied by challenges that need to be addressed prior to considering the potential of the method for in-line inspection. The most significant challenge is the speed at which wafers are imaged. The experimental setup used a 5x objective and wafers are raster scanned to achieve a resolution of approximately 5.5 μm per pixel. In order to meet the time requirements for an in-line inspection method, bowties due to critical microcracks will need to be identified from a full wafer image. As shown in Figure 7.1, to determine the minimum resolution required to identify critical defects we repeatedly computationally reduced the resolution of a bowtie and measured its $\delta_M^{(loc)}$ profile.

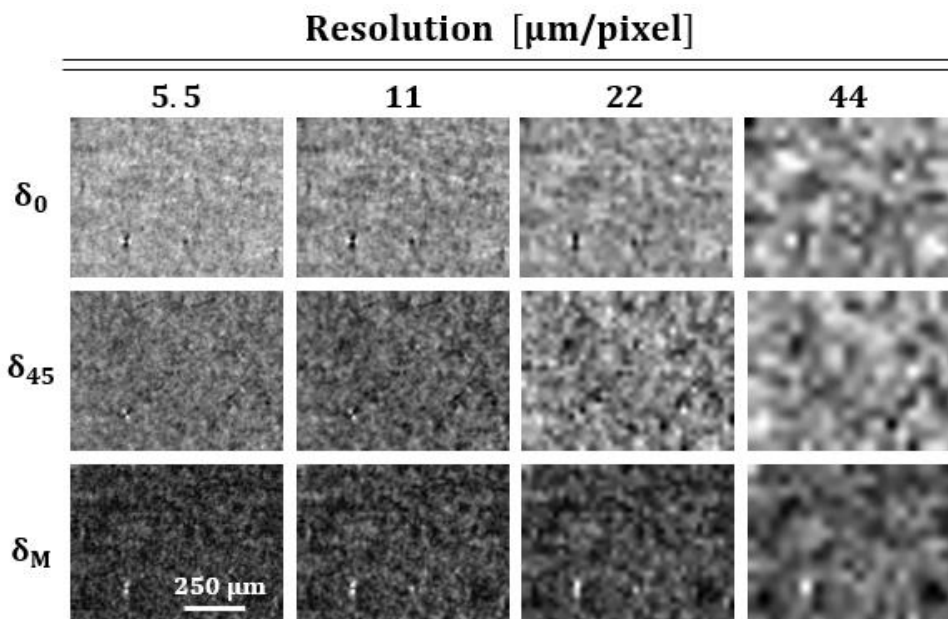


Figure 7.1 Diminishing distinguishability of bowties as resolution is decreased.

The characteristic bowtie profile remains present until the resolution drops between 22 – 44 μm per pixel. Ganapati et al. reported obtaining a resolution of 100 μm per pixel for full wafer view using the same IR-GFP [33]. It is possible that with some work, bowties could be identified from a full wafer image.

This method is dependent on the existing residual stress field to locate microcracks. The intensity of the locally elevated stress fields observed around microcracks depends on the orientation of the microcrack with respect to the bulk residual stress field acting on the crack. As a result, flaws that are approximately orthogonal or parallel to the bulk principal stress direction produce only faint bowtie features and are not characterized. The introduction of a suitably chosen external load can be used to produce locally elevated stress fields from microcracks that, due to their orientation, do not interact with the bulk residual stress field. Special considerations would need to be made when loading and imaging a wafer simultaneously since out-of-plane deformation will defocus the wafer and applying non-contact loads such those described in [10] could result in photoluminescence.

List of references

- [1] C. Hilmersson, D. Hess, W. Dallas and S. Ostapenko, "Crack detection in single-crystalline silicon wafers using impact testing," *Applied Acoustics*, vol. 69, pp. 755-760, 2008.
- [2] Fraunhofer Institute for Solar Energy, "Photovoltaics Report," Freiburg, 2016.
- [3] G. Cellere, H. Forstner, T. Falcon, M. Zwegers, J. Bernreuter and X. G., "International Technology Roadmap for Photovoltaic (ITRPV) 2015 Results Including Maturity Reports," 2015.
- [4] T. Surek, "Progress in U.S. Photovoltaics Looking Back 30 years and Looking Ahead 20," in *3rd World Conference on Phhomvolmic Enera Conversion*, Golden, Colorado, 2003.
- [5] J. Barredo, L. Hermanns, A. Fraile, J. C. Jimeno and E. Alarcon, "Study of the Edge and Surface Cracks Influence," in *24th Eur. Photovolt. Sol. Energy Conference*, Hamburg, Germany, 2009.
- [6] J. Nijs, J. Szlufcik, J. Poortmans, S. Sivothythaman and R. Mertens, "Advanced manufacturing concepts for crystalline silicon solar cells," *IEEE Transactions on Electron Devices*, pp. 1948-1969, 1999.
- [7] K. A. Munzer, K. T. Holdermann, R. E. Schlosser and S. Sterk, "Thin monocrystalline silicon solar cells," *IEEE Transactions on Electron Devices*, pp. 2055-2061, 1999.
- [8] A. Belyaev, "Stress Diagnostics and Crack Detection in Full-Size Silicon Wafers Using Resonance Ultrasonic Vibrations," Tampa, FL, 2005.
- [9] P. Rupnowski and B. Sopori, "Strength of silicon wafers: fracture mechanics approach," *International Journal of Fracture*, pp. 67-74, 2009.
- [10] B. Sopori, P. Sheldon and P. Rupnowski, "Wafer Breakage Mechanism(s) and a," in *Proceedings of the 16th Workshop on Crystalline Silicon Solar Cells and Modules*, Golden, CO, 2006.
- [11] M. Abdelhamid, R. Singh and M. Omar, "Review of Microcrack Detection Techniques," *IEEE Journal of Photovoltaics*, pp. 514-524, 2014.
- [12] C. Klute, F. Kaule and S. Schoenfelder, "Breakage Root Cause Analysis in As-Cut Monocrystalline Silicon Wafers," in *29th European Photovoltaic Solar Energy Conference and Exhibition*, Amsterdam, 2014.
- [13] G. Fisher, M. Seacrist and R. Standley, "Silicon Crystal Growth and," *Proceedings of the IEEE*, vol. 100, pp. 1454-1474, 2012.
- [14] H. Wu, K. Skenes, C. Yang, F. Mess, S. Melkote and S. Danyluk, "Analysis of Slurry and Fixed Abrasive Diamond Wire Sawn Silicon Wafers," in *Crystalline Silicon Workshop*, Breckenridge, CO, 2011.
- [15] H. Möller, C. Funke, M. Rinio and S. Scholz, "Multicrystalline silicon for solar cells," *Thin Solid Films*, pp. 179-187, 2005.
- [16] V. Pogue, "Measurement and analysis of wire sawing induced residual stress in photovoltaic silicon wafers.," Atlanta, GA, 2016.

- [17] C. Yang, H. Wu, S. Melkote and S. Danyluk, "Comparative analysis of fracture strength of slurry and diamond wire sawn multicrystalline silicon solar wafers," *Advanced Engineering Materials*, pp. 358-365, 2013.
- [18] V. Pogue, S. Melkote and S. Danyluk, "Residual stresses in multi-crystalline silicon photovoltaic wafers due to casting and wire sawing," *Materials Science in Semiconductor Processing*, vol. 75, pp. 173-182, 2018.
- [19] G. Fisher, M. Seacrist and R. Standley, "Silicon Crystal Growth and," *Proceedings of the IEEE*, vol. 100, pp. 1454-1474, 2012.
- [20] B. Leroy and C. Plougonven, "Warpage of silicon wafers," *J Electrochem Soc*, vol. 127, pp. 961-970, 1980.
- [21] T. Trupke, J. Nyhus, R. Sinton and J. Weber, "Photoluminescence imaging on silicon bricks," in *Proceedings 24th European Photovoltaic Solar Energy Conference*, Hamburg, Germany, 2009.
- [22] T.-W. Lin, "Characterization of Silicon Photovoltaic Wafers Using Polarized Infrared Imaging," Urbana, 2015.
- [23] M. Demant, S. Rein, J. Krisch, S. Schoenfelder, C. Fischer, S. Bartsch and R. Preu, "Detection and analysis of micro-cracks in multi-crystalline silicon wafers during solar cell production," in *37th IEEE Photovoltaic Specialists Conference*, 2011.
- [24] T. Trupke, R. Bardos, M. Abott, P. Würfel, E. Pink, Y. Augarten, F. Chen, K. Fisher, J. Cotter, M. Kasemann, M. Rüdiger, S. Kontermann, M. Schubert, M. The, S. Glunz, W. Warta, D. Macdonald, J. Tan, A. Cuevas and J. Bauer, "Progress with Luminescence Imaging for Characterization," in *22nd European Photovoltaic Solar Energy Conference*, Milan, Italy, 2007.
- [25] E. Hecht, in *Optics*, San Francisco, CA, Pearson Education, Inc., 2002, pp. 603-606.
- [26] B. Saleh and M. Teich, in *Fundamentals of Photonics*, Hoboken, NJ, John Wiley & Sons, Inc., 2007, pp. 526-528.
- [27] V. Popovich, J. Westra, V. Swaaij, M. Janssen, I. Bennett and R. I.M., "Raman spectroscopy characterization of residual stress in multicrystalline silicon solar wafers and solar cells; relation to microstructure, defects, and processing conditions," in *37th IEEE Photovoltaic Specialists Conference*, Seattle, 2011.
- [28] S. Ostapenko, W. Dallas, D. Hess, O. Polupan and J. Wohlgemuth, "Crack detection and analyses using resonance ultrasonic vibrations in crystalline silicon wafers," in *IEEE 4th World Conference on Photovoltaic Energy*, Waikoloa, HI, 2006.
- [29] A. Belyaev, O. Polupan, W. Dallas, O. Ostapenko, D. Hess and J. Wohlgemuth, "Crack detection and analyses using resonance ultrasonic vibrations in full-size crystalline silicon wafers," *Applied Physics Letters*, no. 88, 2006.
- [30] A. Belyaev, O. Polupan, O. Ostapenko, D. Hess and J. Kalejs, "Resonance ultrasonic vibration diagnostics of elastic stress in full-size silicon wafers," *Semiconductor Science Technology*, vol. 21, pp. 254-260, 2006.

- [31] T. Lin, G. Horn and H. Johnson, "Quantitative infrared photoelasticity of silicon photovoltaic wafers using a discrete dislocation model," *Journal of Applied Mechanics*, vol. 82, 2015.
- [32] R. Inzinga, T. Lin, M. Yadav, H. Johnson and G. Horn, "Characterization and control of residual stress and curvature in anodically bonded devices and substrates with etched features," *Experimental Mechanics*, vol. 52, pp. 637-648, 2012.
- [33] V. Ganapati, S. Schoenfelder, S. Castellanos, S. Oener, R. Koepge, A. Sampson, M. Marcus, B. Lai, H. Morhenn, G. Hahn, J. Bagdahn and T. Buonassisi, "Infrared birefringence imaging of residual stress and bulk defects in multicrystalline silicon," *Journal of Applied Physics*, vol. 108, 2010.
- [34] Stress Photonics Inc., GFP 1400 Operator's Manual, Madison, Wisconsin, 2014.
- [35] G. Horn, J. Lesniak, T. Mackin and B. Boyce, "Infrared grey-field polariscope : A tool for rapid stress analysis in microelectronic materials and devices," *Review of Scientific Instruments*, vol. 76, 2005.
- [36] S. He, T. Zheng and S. Danyluk, "Analysis and determination of the stress-optic coefficients of thin single," *Journal of Applied Physics*, vol. 96, no. 6, pp. 3103-3109, 2004.
- [37] G. Horn, T. Mackin and J. Lesniak, "Trapped particle detection in bonded semiconductors using gray-field photoelastic imaging," *Society for Experimental Mechanics*, vol. 45, no. 5, pp. 457-466, 2005.
- [38] V. Shlyannikov and A. Tumanov, "An inclined surface crack subject to biaxial loading," *International Journal of Solids and Structures*, pp. 1778-1790, 2011.
- [39] V. Shlyannikov, Y. S. Kislova and A. Tumanov, "Mode Mixity Parameters Accounting for Semi-elliptical Surface Crack Behavior," in *Proceedings of the 18th European Conference Fracture*, Dresden, Germany, 2010.
- [40] J. Jaeger, "On Thermal Stresses in Circular Cylinders," *Philos Mag*, pp. 418-428, 1945.
- [41] W. Weibull, *A Statistical Theory of the Strength of Materials*, Ingenjörsvetenskapsakademien, Sweden: Royal Swedish Institute for Engineering Research, 1939.
- [42] T. H. Courtney, *Mechanical Behavior of Materials*, New Delhi, India: McGraw Hill Education, 2013.
- [43] C. Przybilla, A. Fernandez-Canteli and E. Castillo, "Deriving the primary cumulative distribution function of fracture stress for brittle materials from 3- and 4-point bending tests," *Journal of the European Ceramic Society*, vol. 31, pp. 451-460, 2011.
- [44] X. Li, T. Kasai, S. Nakao, T. Ando, M. Shikida, K. Sato and H. Tanaka, "Anisotropy in fracture of single crystal film characterized under uniaxial tensile condition," *Sensors and Actuators*, pp. 143-150, 2005.
- [45] C. Yang, F. Mess, K. Skenes, S. Melkote and S. Danyluk, "On the residual stress and fracture strength of crystalline silicon wafers," *Applied Physics Letters*, 2013.
- [46] R. Koepge, F. Wegert, S. Thormann and S. Schoenfelder, "Characterization of damage and mechanical strength of wafers and cells during the cell manufacturing process," *Photovoltaic Int.*, pp. 55-62, 2013.

- [47] S. Schoenfelder, A. Bohne and B. J., "Comparison of Test Methods for Strength Characterization of Thin Solar Wafers," in *22nd European photovoltaic solar energy conference*, 2007.
- [48] X. F. Brun and S. N. Melkote, "Analysis of stresses and breakage of crystalline silicon wafers during handling and transport," *Solar Energy Materials and Solar Cells*, pp. 1238-1247, 2009.

Appendix – Hypersensitive pixels

A small percentage (0.002 - 0.03%) of pixels in the detector array consistently register abnormally high values. We refer to these pixels as hypersensitive. Throughout the course of each imaging session, in which one wafer is imaged at high resolution, the number of hypersensitive pixels gradually increases. When the detector is allowed to return to thermal equilibrium, the number of hypersensitive pixels resets to zero. While a handful of pixels are always hypersensitive, the collection of hypersensitive pixels is different for each imaging session.

Hypersensitive pixels retain abnormally high values in the subtraction image; if they are not reset to their neighboring pixel values then the hypersensitive pixels will appear in every image. This is problematic because the method we use to detect bowties relies on the fact that the highest pixel values in shear max images occur near the center of bowties.

Hypersensitive pixels generally register as the highest pixel value in the detector array. As such, they can be identified by counting how many times each pixel is the highest valued pixel in the 640 by 480 pixel array out of 3,500 images taken during an imaging session. The probability, p , of a pixel recurring as the highest value pixel can be expressed as

$$p = 1 - \exp\left(-\frac{N!}{n!(N-n)!P^{n-1}}\right) \quad (\text{A.1})$$

where n is the number of times the pixel is the highest value pixel in an image, N is the total number of images, and P is the number of pixels in each image. Thus, the probability of a pixel having the highest value in 3, 4, and 5 images is respectively 7.3, 0.02, and 4.9E-5 percent. Any pixel occurring as the highest pixel in an image 5 or more times in a single imaging session is flagged as a hypersensitive pixel and reset to the average value of its neighboring pixels. Since some images contain more than one hypersensitive pixel, the process of identifying and resetting hypersensitive pixels is repeated until no new hypersensitive pixels are identified.